UNIVERSITY OF CRETE

DEPARTMENT OF MATERIALS SCIENCE AND TECHNOLOGY

Electronic and optical properties of ZnX(X:S,Se,Te) and $Mn_xZn_yNi_yO_4$: A first principles investigation

Emmanouil Pervolarakis

Thesis Committee:

Ioannis N. Remediakis (Supervisor)

Georgios Kopidakis

Constantinos C. Stoumpos

Heraklion, June 2020

A thesis submitted in partial fulfilment of the requirements of the degree of:
Master of Science in Materials Science and Technology

Abstract

Zinc is a common material that is often used in modern materials due to its abundance, low price, non-toxicity, material stability and its great ability to alloy with most metallic elements. Zinc-containing oxides and chalcogenides are used extensively in a variety of applications. In this thesis, we consider two characteristic families of Zn-based materials: Zn chalcogenides and Zn-doped Mn_2NiO_4.

The Zn-chalcogenide family of materials (ZnS, ZnSe, ZnTe) are direct gap II-VI semiconductors which are excellent base materials for optical device technology due to their large gap and optical properties. Mn_2NiO_4, on the other hand, is a well-known material as a temperature sensor thanks to its negative temperature coefficient of resistance (NTCR) but its alloys with Zn require further investigation. In this thesis, we employ density functional theory (DFT) in the Projector-Augmented Wave (PAW) implementation to calculate the electronic structure and characteristic properties of these materials.

In the first part of the thesis we probe the structural, electronic and optical properties of the Zn chalcogenide family of materials using first principles calculations. Even though DFT can produce really accurate results for the ground state, it falls short when it comes to excited state properties like the semiconductor band-gap and the absorption spectrum. For a more accurate description, we solve the Bethe-Salpeter Equation in the GW approximation in order to include many-body effects in our calculations that arise from the electron-hole interactions like excitons.

The second part of this thesis revolves around Mn_2NiO_4 and its alloying by the Zn substitution of Mn. We calculate the ground state structure, magnetization and density of states of these materials for various concentrations Zn. We then proceed to calculate the properties of two similar material series of the $Mn_xZn_yNi_zO_4$ type. Although these alloys have very promising electronic properties, detailed simulations as well as experiments are missing. In close collaboration with experimental colleagues, we will unravel the potential of these materials for sensing applications.

Contents

CHAPTER 1

Introduction

This thesis revolves around calculations performed for Zn compounds and Zn-containing materials. The calculations were carried out using Density Functional Theory(DFT) and some post-DFT schemes for properties where DFT falls short. Among the Zn compounds the focus was the family of Zn chalcogenides ZnX, with X being sulfur, selenium or tellurium, and alloys of the form $Mn_{2.5-x}Zn_xNi_{0.5}O_4$ and $Mn_{2.5-x}Zn_{0.5}Ni_xO_4$. All of the materials of interest in this thesis are also investigated by two different groups of experimental colleagues.

1.1 Zn and its compounds

Zn(atomic number: 30) is a relatively abundant element in the earth's crust, more abundant than copper that is used widely in its bulk form. It is a transition metal with electronic configuration: $[Ar]3d^{10}4s^2$. In its metallic form it is used for anti-rust coatings for steel or iron thanks to its easy oxidation, but it can also form a plethora of compounds with very interesting properties, and especially in the nano-materials community it has attracted a lot of attention. One of the most famous Zn-nanomaterials is ZnO, a semiconductor with direct band-gap $\approx$ 3eV that has been studied in a wide range of applications from photocatalysis to sensors and supercapacitors [1][2].

Directly bellow O in its periodic table group follow the chalcogens, S, Se and Te. Their Zn compounds , namely ZnS, ZnSe and ZnTe have very interesting optical and electronic properties. Like ZnO they are all direct-band gap semiconductors, a much coveted property for opto-electronical applications, with band gaps ranging from $\approx 2.2 - 3.6$eV. They belong to the II-VI semiconductor family and being wide-gap semiconductors they have

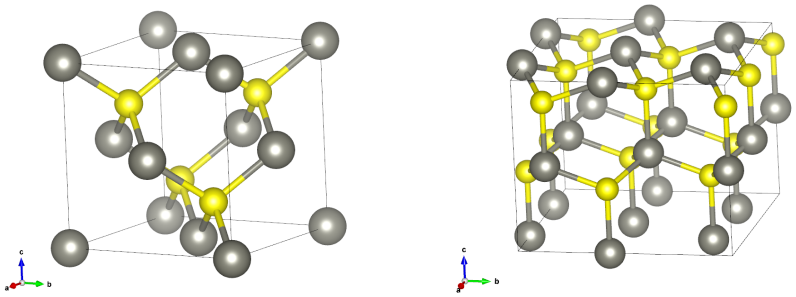

Figure 1.1: The two primitive cells of the structures that the ZnX materials can be found. Left: The more stable at room temperature Zinc-Blende structure, Right: The wurtzite structure.

attracted the interest of researchers to study their optoelectronic properties, especially as blue-lasing materials. Nowadays their nanostructures [3] are also being investigated and some groups have even managed to synthesize them in layered form [4] and are studied in a plethora of applications. They crystallize in the cubic zincblende structure at lower temperatures but can be synthesized in their hexagonal wurtzite structure as well [5]. The atomic structure of the Zinc-Blende and Wurtzite can be seen in Fig. 1.1

In the first part of this thesis the optical properties of these materials are going to be investigated from first-principles with the goal of recreating their optical absorption spectra. The results of this part will be presented in Chapter 4.

Another Zn material, not as popular but a very interesting one is the tetragonal spinel Mn_2ZnO_4. It has been studied as a potential candidate for a range of energy and energy storage applications like supercapacitors [6], for Lithium-Ion batteries[7] and as a catalyst for the production of biofuel [8].

A similar material to Mn_2ZnO_4 is Mn_2NiO_4 that crystallizes in the cubic spinel structure and its mostly known as a temperature sensor material thanks to its negative temperature coefficient of resistance, good response and low cost [9][10].

Doping-alloying ,depending on the percentage of the introduced element to the parent material, is well-known method to improve a material's properties. The effect of Zn and Ni introduced in the $Mn_{2.5}Ni_{0.5}O_4$ and $Mn_{2.5}Zn_{0.5}O_4$ structures respectively is going to be explored. The results will be presented in Chapter 5.

1.2 Computational Materials Science

Humans always tended to find ways to predict how a situation would evolve, this was an evolutionary perk since by being better prepared they had better chances of survival.

Computational materials science is no different from that human need, its objective is the prediction of how certain materials would respond in different situations. This gives an edge to society since by being able to reproduce experimental results and even predict the properties of unknown materials saves time from experimental researchers and of course money and the natural resources that would be otherwise used in the experiments. Computational materials science researchers are in essence no different from their experimental colleagues, they just conduct virtual experiments. Additionally, in the virtual experiments one can delve deeper and investigate some properties that are not easily measured experimentally due to equipment limitations. The computational materials scientist on the other hand can create the *"perfect experiment"*, which is not always good of course because in the real world the conditions are hardly ever that ideal and due to computational limitations it is not always easy to recreate the imperfections of the real world.

There are various tools that make those virtual experiments in materials science, depending on the level of theory one is interested in. Ab-initio calculations use quantum-mechanics to reproduce very accurate experimental results but due to the computational load the amount of atoms/electrons that can be included in the calculations is quite limited. Then there are Monte-Carlo simulations that are more widely used for molecular and fluid calculations and there are also computer programs for whole device designing. In this thesis only ab-initio calculations were performed.

The most widely used method to study the ground state properties of materials from first principles is Density Functional Theory (DFT). Examples of such properties are their structure, their elastic constants and their density of states. In order to study excited states of the materials, like optical excitations, at this level of theory DFT is not enough. The theoretical groundwork of these methods will be discussed in the following Chapter.

CHAPTER 2

Theory

2.1 The many electron problem

In the next two chapters some theoretical and computational concepts will be introduced. The content of these chapters was greatly influenced by two books, *Solid State Physics: A shortened version* by E. N. Economou [11] and *Computational Physics* by J. Thijssen[12].

Since most of the ground state properties of materials are governed by the behaviour of the material in the quantum level , the Schrödinger's equation (Eq. 2.1) needs to be solved for all the volume of the material in order to calculate these properties.

$$\hat{H}\psi = E\psi \tag{2.1}$$

$\hat{H}$ is the Hamiltonian of the system ,which in this case consists of N electrons and K nuclei. It takes the form:

$$\begin{aligned}\hat{H} =& \sum_{i=1}^{N} \frac{\hat{p}_i^2}{2m} + \sum_{n=1}^{K} \frac{\hat{P}_n^2}{2M_n} + \frac{1}{4\pi\epsilon_0}\frac{1}{2}\sum_{i,j=1;i\neq j}^{N} \frac{e^2}{\mid \mathbf{r}_i - \mathbf{r}_j \mid} \\ & - \frac{1}{4\pi\epsilon_0}\frac{1}{2}\sum_{n=1}^{K}\sum_{i=1}^{N} \frac{Z_n e^2}{\mid \mathbf{r}_i - \mathbf{R}_n \mid} + \frac{1}{4\pi\epsilon_0}\frac{1}{2}\sum_{n,n'=1;n\neq n'}^{N} \frac{Z_n^2 e^2}{\mid \mathbf{R}_n - \mathbf{R_n}' \mid}\end{aligned} \tag{2.2}$$

In the above equation, indices i and n refer to the electrons and nuclei respectively, m refers to the electron mass and M_n refers to the mass of the nucleus n. The first and third term describe the kinetic energy and Coulomb interaction of the electrons respectively, the second and fifth term describe the kinetic energy and Coulomb interaction of the ions respectively and the fourth term describes the Coulomb interaction between the electrons and the nuclei. The 1/2 in the coulomb terms is accounting for doulbe-counting.

From Eq.(2.1) and Eq.(2.2) it is deduced that the wavefunction of the system is dependent upon the positions of both electrons and nuclei. This problem is impossible to solve even with state-of the art computer systems and doesn't seem it will be possible in the near future. In order to tackle this obstacle some drastic approximations need to be made.

2.2 Basic Approximations

A first simplification that can be made is the disentanglement of the electronic and ionic degrees of freedom. This approximation is called the Born-Oppenheimer approximation and is well justified by the fact that one proton is ≈ 2000 times heavier than the electron, thus the nuclei are moving much slower and by the time they have moved, the electrons will have already adjusted their positions and hence the nuclei seem static to the electrons. The new Hamiltonian of the electrons takes the form:

$$\hat{H}_{BO} = \sum_{i=1}^{N} \frac{\hat{p}_i^2}{2m} + \frac{1}{4\pi\epsilon_0}\frac{1}{2}\sum_{i,j=1;i\neq j}^{N} \frac{e^2}{\mid \mathbf{r}_i - \mathbf{r}_j \mid} - \frac{1}{4\pi\epsilon_0}\frac{1}{2}\sum_{n=1}^{K}\sum_{i=1}^{N} \frac{Z_n e^2}{\mid \mathbf{r}_i - \mathbf{R}_n \mid} \tag{2.3}$$

while the nuclei are treated separately and the total energy will be the sum of the energy of the nuclei and that of the electrons.

Even though the Born-Oppenheimer approximation lightens the load considerably, the second term of Eq.(2.3) is still too much to handle and at this point a really drastic approximation needs to be made.

The Independent Particle approximation does the trick by considering the movement of one electron independent of the rest in a potential that is determined in a self-consistent manner that arises from the other moving electrons and the static nuclei. With this approximation the previously impossible problem becomes that of solving Eq.(2.1) for one particle N times, which is feasible. The problem now for one electron takes the form:

$$-\frac{\hbar^2}{2m}\nabla^2\psi(\mathbf{r}) + \hat{\mathcal{V}}(\mathbf{r})\psi(\mathbf{r}) = E\psi(\mathbf{r}) \tag{2.4}$$

For the electron system, the Hamiltonian is:

$$\hat{H}_{IP} = \sum_{i=1}^{N} \left[\frac{\hat{p}_i^2}{2m} + \hat{\mathcal{V}}(\mathbf{r}) \right] \tag{2.5}$$

The problem now lies in finding the potential $\hat{\mathcal{V}}$ which is not a trivial task. This operator depends on the wavefunction on which it is acting on and is non-local as it is affected by the positions of the other electrons of the system. There are methods to solve this problem like the Hartree-Fock(HF) method, a variational approach, and Density Functional Theory(DFT). In this thesis, DFT was exclusively used and it's going to be described in the next section.

2.3 Density Functional Theory

DFT was first developed by the works of Hohenberg and Kohn [13] and Kohn and Sham [14] and since then it has become a prominent tool in the computational materials science community. In [13] is proved that the ground state of an interacting electron gas is a unique functional of the electron density.

$$E = E\left[n(\mathbf{r})\right] \tag{2.6}$$

They defined the electron density of the ground state of N electrons as:

$$n(\mathbf{r}) \equiv \sum_{i=1}^{N} \mid \psi_i(\mathbf{r}) \mid^2, \tag{2.7}$$

and the results of their work showed that the density functional that minimizes the energy is the one that describes the ground state, so a self-consistent scheme can be applied to find this electron density, the energy and a wide range of ground state properties that depend on the energy. In order to apply this self-consistent scheme, the electron density needs to updated, something that is achieved by solving an Independent Particle Schödinger's equation for the electrons of the system known as the Kohn-Sham Equation Eq.(2.8)

$$\left[-\frac{\hbar}{2m}\nabla^2 + \hat{V}(\mathbf{r}) + \hat{V}_H(\mathbf{r}) + \hat{V}_{xc}(\mathbf{r}) \right] \psi_i(\mathbf{r}) = \varepsilon_i \psi_i(\mathbf{r}) \tag{2.8}$$

With:

$$\hat{V}_H = \frac{e^2}{4\pi\epsilon_0} \int d^3r' n(\mathbf{r}') \frac{1}{\mid \mathbf{r} - \mathbf{r}' \mid} \tag{2.9}$$

In Eq.(2.8) the first term is the electronic kinetic energy operator, the second is the electrostatic potential of the nuclei-electrons interaction, the third term, also known as

Hartree potential Eq.(2.9), is just the non-interacting electron-electron interaction. All the quantum mechanical effects like exchange and self-interaction are lumped in the last term. It is obvious that the Born-Oppenheimer approximation has been taken into account since the kinetic energy and Coulomb interaction of the ions is missing.

In order to apply this self-consistency scheme, a trial electron density is used. With this density Eq.(2.8) is solved and from the electron wavefunctions that are found, a new electron density is calculated from Eq.(2.7), if this new density n is different than the trial, the same procedure is repeated until the convergence criteria are fulfilled. Then all that is left to do is calculate the total ground state energy that is given by:

$$E = \sum_{k=1}^{N} \varepsilon_k - \frac{1}{2}\frac{1}{4\pi\epsilon_0}\int d^3r d^3r' \, n(\mathbf{r})\frac{1}{\mid \mathbf{r}-\mathbf{r}' \mid} n(\mathbf{r}) + E_{xc}\left[n\right] - \int d^3r V_{xc}\left[n\right] n(\mathbf{r}) \quad (2.10)$$

with:

$$V_{xc}\left[n\right] = \frac{\delta}{\delta n} E_{xc}\left[n\right] \quad (2.11)$$

The exact form of the exchange and correlation term is unknown but further approximations are made to tackle this problem.

2.3.1 Local Density Approximation(LDA)

In the LDA the exchange and correlation potential is approximated by an XC potential of a homogeneous electron gas that depends only on the electronic density and the exchange-correlation energy per particle of the gas Eq.(2.12). This approximation holds well for systems that their electron density doesn't vary quickly.

$$E_{xc} = \int d^3r \varepsilon_{xc}\left[n(\mathbf{r})\right] n(\mathbf{r}) \quad (2.12)$$

2.3.2 Generalized Gradient Approximation(GGA)

GGA, in addition to the electron density, takes into consideration the former's gradient, making it a more suitable approximation for systems with more rapidly changing electronic density (e.g. a surface) Eq.(2.13).

$$E_{xc} = \int d^3r \varepsilon_{xc}\left[n(\mathbf{r}), \nabla n(\mathbf{r}))\right] n(\mathbf{r}) \quad (2.13)$$

Purdew, Burke and Ernzerhof [15] in their work modified the GGA by introducing an enhancement factor F_{xc} to include non-locality effects. Eq.(2.14)

$$E_{xc} = \int d^3r \varepsilon_x^{unif} \left[n(\mathbf{r})\right] n(\mathbf{r}) F_{xc}(r_s, s) \tag{2.14}$$

in which:

r_s is the Seitz radius: $r_s = \sqrt[3]{\frac{3}{4\pi n}}$

s is a density gradient: $s = \frac{\nabla n}{2k_F n}$ and k_F is the Fermi wavevector: $k_F = \sqrt[3]{3\pi^2 n}$

2.4 Post-DFT Methods

Even though DFT is extremely useful in calculating the ground state properties of materials it falls short when it comes to excited states. The eigenvalues of the Kohn-Sham Equations Eq.(2.8) are lagrangian multipliers, a mathematical tool to solve our problem, but they bear no physical meaning and aren't accurate for describing electron addition or extraction energies. The above statement is also supported by the well-known inadequacy of DFT in calculating energy band-gaps which it greatly underestimates (see Fig. 2.1).

The single-particle excitation energies can be calculated by the Green function theory which shows that the quasiparticle energies are given by:

$$\left[-\frac{1}{2}\nabla^2(\mathbf{r}) + \hat{V}_H(\mathbf{r})\right] \Psi_i(\mathbf{r}) + \int d^3r' \hat{\Sigma}(\mathbf{r}, \mathbf{r}'; E_i)\Psi_i(\mathbf{r}') = E_i \Psi_i(\mathbf{r}) \tag{2.15}$$

$\hat{\Sigma}$ in Eq.(2.15) is the complex self-energy operator and it contains the exchange and correlation effects while here Ψ_i is the all-electron wavefunction. Notice that it is non-local and energy dependent making it very difficult to calculate, so more approximations are in order. Such an approximation is the GW approximation that will be discussed in the next section and some of its results showcasing its success can be seen in Fig. 2.1.

2.4.1 GW Approximation (GWA)

GWA is a result of many-body pertubation theory and is based heavily on the work of Hedin [17] who performed the first self-energy calculation with GWA for the electron gas. It wasn't until 1985 that it was used by Hybertsen and Louie[18] for real material calculations because it is computationally demanding.

In the GW approximation the self-energy introduced in Eq.(2.15) is approximated by an integral of GW where G is the Green's function and W the screened Coulomb potential between electrons. In practice G is easily calculated from the single particle wavefunctions using Eq. (2.16) in which a represent one electron orbitals (for this reason GWA is uses DFT calculations as its base) and is solved at the limit $\delta \to 0$. The screened

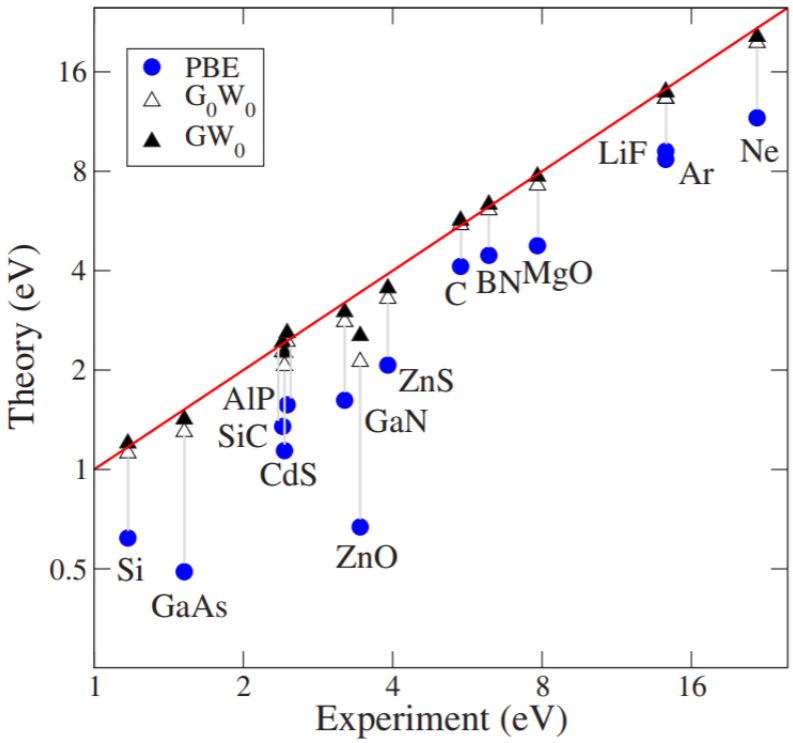

Figure 2.1: Band Gap values for a variety of materials obtained by PBE, G_0W_0 and GW_0. The experimental values lie on the red line, the DFT values are represented by circles while the G_0W_0 and GW_0 values are represented by the white and black triangles respectively. Figure obtained from Ref. [16]

Coulomb potential is just the bare Coulomb potential divided by the dielectric function of the material.

$$G(\mathbf{r}, \mathbf{r}', \omega) = \sum_a \frac{\psi_a(\mathbf{r})\psi_a(\mathbf{r}')}{\omega - E_a - i\delta} \tag{2.16}$$

A more formal description of the GWA will be provided here. It is based on the Green's function theory. The Green's function of an electron (at zero temperature) is defined as an expectation value to the many-electron ground state [19]:

$$G(xt, x't') = -i\langle N \mid \hat{T}\psi(xt)\psi^\dagger(x't') \mid N\rangle \tag{2.17}$$

In Eq(2.17): x describes three three spatial coordinates ($\mathbf{r}$) and the spin of a particle, T is the time-ordering operator, $\psi^\dagger \mid N\rangle$ describes the system with an additional electron that was introduced in point $\mathbf{r}$ and time t. If $t' < t$, G gives the probability amplitude

to find an electron at point $\mathbf{r}$ and time t if an electron was added at point $r^{'}$ and time $t^{'}$. If $t < t^{'}$ the state describes electron removal and the propagation of a hole [19].

The core of the approximation can be found in the Hedin's Equations that link the self-energy with the screened Coulomb interaction, the polarizability, the Green's Function and a Vertex function.

$$\Gamma(1,2;3) = \delta(1,2)\delta(1,3) + \int d4d5d6d7 \frac{\mathrm{e}lta\Sigma(1,2)}{\delta G(4,5)} \times G(4,6)G(7,5)\Gamma(6,7;3) \tag{2.18}$$

$$P(1,2) = -i \int d(34)G(1,3)\Gamma(3,4;2)G(4,1^{+}) \tag{2.19}$$

$$W(1,2) = \upsilon(1,2) + \int d(34)\upsilon(1,3)P(34)W(4,2) \tag{2.20}$$

$$\Sigma(1,2) = i \int d(34)G(1,3)\Gamma(3,2;4)W(4,1^{+}) \tag{2.21}$$

$$G(1,2) = G_0(1,2) + \int d(34)G_0(1,3)\Sigma(3,4)G(4,2) \tag{2.22}$$

In the above equations $1 \equiv (\mathbf{r_1}, \sigma_1, t_1)$ and $1^{+} \equiv (\mathbf{r_1}, \sigma_1, t_1 + \delta t)$, $2 \equiv (\mathbf{r_2}, \sigma_2, t_2)$ and $2^{+} \equiv (\mathbf{r_2}, \sigma_2, t_2 + \delta t)$ and so on with δ a positive infinitesimal. The υ denotes the bare (unscreened) Coulomb interaction and P is the irreducible polarizability that is used in the calculation of the screened Coulomb interaction ,W , and Γ is a vertex function that contains information that the electron and hole interact. Their derivation can be found in Hedin's paper [17].

So far no approximation has been made. The more challenging equation from the above is the vertex function the second term of which is a 20th dimension integral. GWA neglects vertex corrections leading thus to a simplified form of the above equations:

$$\Gamma(1,2;3) = \delta(1,2)\delta(1,3) \tag{2.23}$$

$$P(1,2) = -iG(1,2)G(2,1^{+}) \tag{2.24}$$

Note: Polarizability in this form is the Random Phase Approximation.

$$\Sigma(1,2) = iG(1,3)W(3,1^{+}) \tag{2.25}$$

Σ needs to be calculated self-consistently which is no-easy task but at least is feasible. Even with just 1 iteration (known as G_0W_0, can be seen in Fig.2.4) it yields results much closer to the experiment than PBE. G_0 can be calculated from an ordinary DFT calculation. Eq. (2.15) now can be solved with the self-energy operator from GWA. The eigenvalues as mentioned before are complex, with the real part being the quasiparticle energies and the imaginary part being the excited state lifetime.

2.4.2 Bethe-Salpeter Equation

In the GWA the vertex corrections were neglected treating this way the quasi-electron and a quasi-hole as non-interacting, but in reality they do interact since they have opposite charges and attract each other. In bulk materials this interaction is greatly quenched by the surrounding electrons but it is particularly strong in 2-D materials that can be of the order of 0.5 eV. The quasiparticle formed by an electron and a hole is named an exciton and its energy cannot be calculated in the GWA. Optical absorption is a two-particle process and even though in the RPA we can calculate an absorption spectrum(from GWA calculations) it is not an adequate approximation for many materials.

The Bethe-Salpeter Equation(BSE) can be used in addition to GW to calculate the two-quasiparticle (e.g. an exciton's) eigenergies. BSE is a 4-point equation and can be seen in Eq.(2.26).

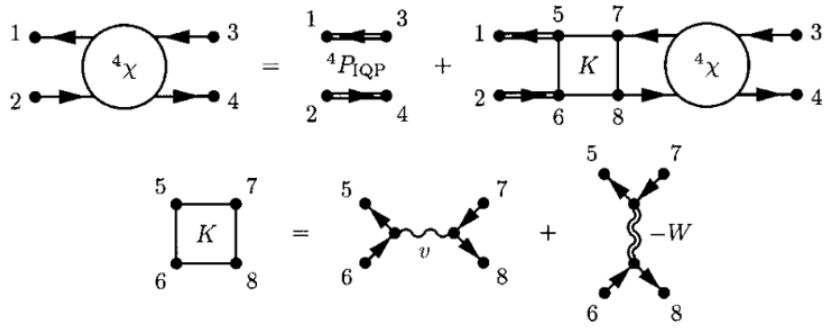

Figure 2.2: The Bethe-Salpeter equation shown by Feynman Diagrams. Single straight lines with arrows represent the non-interacting Green's Functions, the double straight lines represent the interacting Green's Functions, the single wiggly line represents the bare Coulomb interaction and finally the double wiggly line represents the screened Coulomb interaction. Figure taken from [19]

The equation in mathematical form is:

$$\begin{gathered}\chi(1,2,3,4) = \chi^0(1,2,3,4) + \int d(5678)\chi^0(1,2,3,4)K(5,6,7,8)\chi(7,8,3,4) \\ K = V - W = V_H(5,7)\delta(5,6)\delta(7,8) - W(5,6)\delta(5,7)\delta(6,8)\end{gathered} \tag{2.26}$$

χ is the density response function and Eq.(2.26) with some mathematical tricks can lead to an effective two particle Hamiltonian making it possible to calculate the eigenvalues and eigenvectors. χ is also directly related to the dielectric function , e.g. in Eq. (2.27), from the imaginary part of which one can create optical spectra.

$$\epsilon = (1 + \chi)\epsilon_0 \tag{2.27}$$

CHAPTER 3

Computational Methods

This chapter aspires to provide a short introduction to some concepts used in our calculations and will be referred to in the next two chapters. In Chapter 2 the basic theoretical concepts upon which DFT and post-DFT methods were built upon were introduced, but there is a lot that hasn't been mentioned about the computational approach to solve these problems.

3.1 Plane waves and Bloch Theorem

As was briefly mentioned in the previous chapter, the calculation needs to include all the material volume. This is absurdly difficult for a real material since just 1 mole of it has atoms of the order of 10^{23} and one to two orders higher number of electrons. To tackle this problem the Bloch's Theorem is used for large systems in which some form of periodicity can be found (atoms in bulk materials are organized periodically). Because the arrangement of the atoms is periodic the electrostatic potential of the nuclei will be periodic as well: $V(\mathbf{r}) = V(\mathbf{r} + \mathbf{R_n})$ with $\mathbf{R_n}$ any translation vector of the crystal lattice.

By using Bloch's theorem and the periodicity of the system the number of particles for which the Schrödinger's equation needs to be solved is dramatically reduced to just the number of particles in a cell that if repeated infinitely, will reproduce the material. The wavefunction of the system can then take the form:

$$\psi(\mathbf{r}) = e^{i\mathbf{kr}} u(\mathbf{r}), \tag{3.1}$$

where u is a periodic function with the periodicity of the cell and it can be expanded in plane waves:

$$u(\mathbf{r}) = \sum_{\mathbf{G}'} \tilde{u}(\mathbf{G}')e^{i\mathbf{G}'\mathbf{r}} \tag{3.2}$$

So the wavefucntion becomes:

$$\psi(\mathbf{r}) = \sum_{G'} \tilde{u}(\mathbf{G}')e^{i(k+\mathbf{G}')\mathbf{r}} \tag{3.3}$$

G in Eq.(3.2) are the reciprocal lattice vectors. More on the reciprocal lattice will be mentioned in the final section of this Chapter.

Using Eq. (3.3) and assuming a similar form for the periodic potential of the solid in the independent particle hamiltonial Eq.(2.5):

$$-\frac{\hbar^2(k+G)^2}{2m}\tilde{u}(\mathbf{G}) + \sum_{\mathbf{G}'} \tilde{u}(\mathbf{G}')\tilde{v}(\mathbf{G}-\mathbf{G}') = E\tilde{u}(\mathbf{G}) \tag{3.4}$$

Another problem that needs to be addressed is the basis in which the wavefunctions will be expressed. The obvious choice is a Plane Wave basis set since it's a simple one and occurred naturally in the Bloch wavefunction. In order to have the correct prediction the basis set should be infinite but this of course is not feasible for numerical solutions and hence a limit needs to be found that will have a certain degree of accuracy.

This limit is referred to as the Plane-wave cutoff energy and it represents the maximum reciprocal vector included in the calculation. $\mid G + k \mid < G_{cut}$. The reciprocal vectors represent momentum and finally the cutoff energy is given by:

$$E_{cut} = \frac{\hbar^2}{2m}{G_{cut}}^2 \tag{3.5}$$

3.2 Pseudopotentials and the Projector Augmented Wave method

With the above formulation everything looks fine at first but there are yet problems that need to be tackled. The wavefunctions span through all the calculation space, even inside the nuclei (or ions if some of the inner electrons are considered inert). That is quite a challenging area to treat due to the $1/r$ dependence of the potential and hence for $r < r_c$ where r_c is the radius of a nucleus/ion. In this region, the wavefunction behaves quite peculiar and needs a much larger basis to be correctly described, which is not an appealing prospect since this would mean increased computation time.

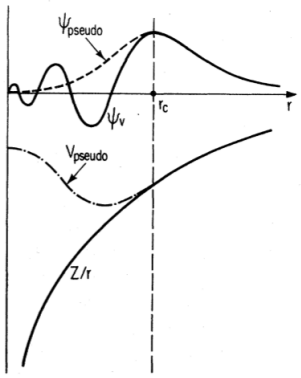

Figure 3.1: The wavefunction and the potential in contrast to the pseudo-potential and the pseudo-wavefunction. Figure taken from [20]

This oscilation of the wavefunction was treated with a variety of approaches one of which is the pseudo-potential method which focuses on finding a potential that will reproduce the energy eigenvalues and the wavefunctions for $r > r_c$ and that the wavefunctions calculated for $r < r_c$ to be smooth and without any points that the wavefunction is zero. This technique is well justified since the core(nucleus/ion) is not participating in chemical bonding and most of the material properties. The method is depicted in Fig. 3.1.

In the calculation, most of the core electrons are lumped with the nucleus since they don't participate in bond formation and can be considered as inert. The r_c then refers to a radius that determines for which electrons the Schrödinger's equation will be solved.

A generalization of the pseudo-potential method and a more accurate method is the Projector-Augmented Wave that was introduced by Blöchl [21]. PAW uses the same idea to use an auxiliary wavefunction for the core that can be more computationally efficient but uses a transformation operation, like in Eq.(3.6), to map the pseudo to the true electron wave function. Then, only the transformed Kohn-Sham equation, Eq. (3.7) needs to be solved and of course the transformation operator $\mathcal{T}$ needs to be determined. $\mathcal{T}$ is the transformation operator and n represents a quantum state.

$$\mid \psi_n\rangle = \hat{\mathcal{T}} \mid \tilde{\psi}_n\rangle \tag{3.6}$$

$$\hat{\mathcal{T}}^\dagger \hat{H} \hat{\mathcal{T}} \mid \tilde{\psi}_n\rangle = \epsilon_n \hat{\mathcal{T}}^\dagger \hat{\mathcal{T}} \mid \tilde{\psi}_n\rangle \tag{3.7}$$

3.3 K-point grid

Due to the periodicity of the lattice and Bloch's theorem, the wavefunction is the same for a translation $\mathbf{r} \rightarrow \mathbf{r} + \mathbf{R_n}$ with $\mathbf{R_n} = n_1\mathbf{a_1} + n_2\mathbf{a_2} + n_3\mathbf{a_3}$ where the three n are integers and the three $\mathbf{a}$ are the cell's basis vectors.

$$\psi(\mathbf{r} + \mathbf{R_n}) = e^{i\mathbf{k}\mathbf{R_n}}\psi(\mathbf{r}) \tag{3.8}$$

From the above equation it follows that the value of the wavefunction will be repeated for $\mathbf{k} = \mathbf{k} + \mathbf{G_m}$ where

$$\mathbf{G_m} = \frac{2l\pi}{\mathbf{R_n}}, \text{l integer} \tag{3.9}$$

The $\mathbf{G_m}$ wavevectors are given by:

$$\mathbf{G_m} = m_1\mathbf{b_1} + m_2\mathbf{b_2} + m_3\mathbf{b_3},\ m_1, m_2, m_3 \text{ integers, and} \tag{3.10}$$

$$\mathbf{b_1} \equiv 2\pi\frac{\mathbf{a_2} \times \mathbf{a_3}}{\mathbf{a_1} \cdot (\mathbf{a_2} \times \mathbf{a_3})},\ \mathbf{b_2} \equiv 2\pi\frac{\mathbf{a_3} \times \mathbf{a_1}}{\mathbf{a_2} \cdot (\mathbf{a_3} \times \mathbf{a_1})},\ \mathbf{b_3} \equiv 2\pi\frac{\mathbf{a_1} \times \mathbf{a_2}}{\mathbf{a_3} \cdot (\mathbf{a_1} \times \mathbf{a_2})} \tag{3.11}$$

Where $\mathbf{b_1}$, $\mathbf{b_2}$ and $\mathbf{b_3}$ are basis vectors that form the reciprocal lattice. The volume in the reciprocal lattice defined by its three basis vectors is called the first Brilluin Zone and the important thing is that if we calculate the wavefunctions in this area we know how all of the material will behave. Of course it is not possible to make the calculations for every point in this zone since there are infinite points, so a grid is used. The finer the grid the more accurate the calculation. Usually the grid is formed by specifying how many divisions should be made in the reciprocal basis vectors, e.g. a possible grid would be $5 \times 5 \times 5$ that would give a total of 125 reciprocal points (k-points) included. Due to symmetry reasons some of the points are recurring so they are usually excluded and the number of k-points included are reduced. These final points are called irreducible k-points.

All the calculations performed in this thesis were performed using DFT in the PAW method as is implemented by the Vienna ab initio simulation package (VASP version 5.4.4), all the k-point grids used were Γ centered Monkhorst-pack grids and the PBE(Purdew-Burke-Ernzerhof) exchange and correlation functional was used for the ground state calculations. Our calculations were converged in terms of plane-wave cut-off energy, number of bands and k-point grid sampling.

3.4 Computational details for the GWA and BSE

The BSE is solved on a GWA calculation based on a DFT calculation. We find Fig. 3.2 quite enlightening as to how GW and BSE calculations are conducted. The one-electron wavefunctions and eigenenergies are used to calculate G from Eq.(2.16). Then using Hedin's equations the polarizability is calculated which is related to the response function χ which in turn is related to the dielectric function which it is finally used for the screened Coulomb interaction W. W together with G are used to calculate the self-energy which is used to solve the effective Schrödinger's Eq.(2.15) and obtain the energy eigenvalues. The eigenenergies, the one-electron orbitals (that might be updated in some GW types) and the screened coulomb interaction are required for solving the BSE.

The GWA can be used in many different ways, we tested three of them. We follow the abreviations used by VASP. The most common one is the G_0W_0 in which both G and W are calculated only once, without any self-consistency scheme. Then there is the partially self-consistent GW_0 calculations in which W is still calculated from DFT but G is updated self-consistently in respect to the eigenvalues but it still uses the same DFT wavefunctions. And finally the third flavour of GWA that we used is the self-consistent $QPGW_0$ which in addition to the eigenenergies, the wavefunctions are also updated but again W remains unchanged.

There are a number of parameters used in a GW calculation. The ones that will be mentioned in the thesis will be explained briefly:

ENCUTGW: It stands for the energy cutoff of the basis set used for the calculation of the response function χ and works as the plane wave cutoff energy.

NBANDSV: This parameter determines the number of virtual orbitals (or unoccupied orbitals) in the calculation.

NOMEGA : It specifies the number of frequency points considered in the frequency integration (G is frequency dependent hence we integrate for frequency too for the self-energy.)

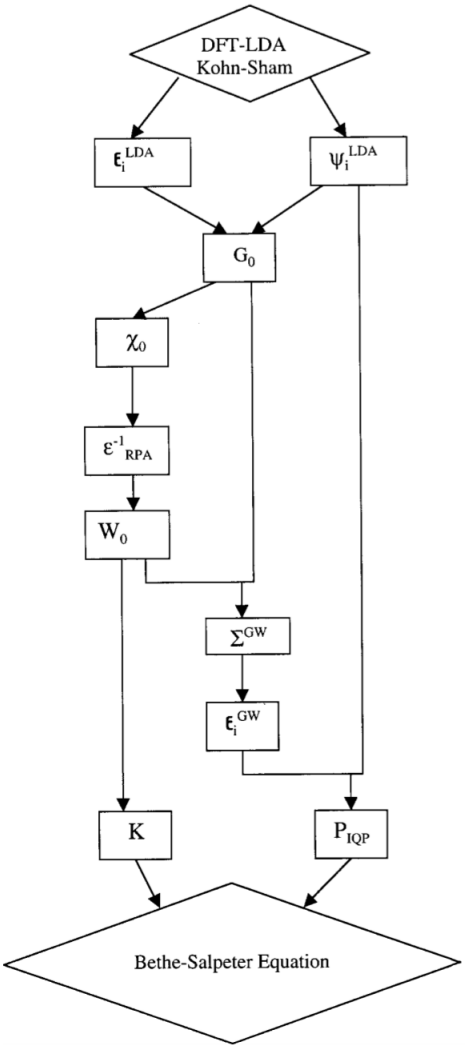

Figure 3.2: Schematic representation of the workflow of a BSE calculation. Figure obtained from ref. [19].

CHAPTER 4

Optical Properties of Zn chalcogenides

In this chapter the end goal was the calculation of the absorption spectra of ZnS, ZnSe and ZnTe, but along the way some other properties of these materials were calculated. At the beginning the structure of the materials was determined, then their Bandstructure was calculated and finally the GW approximation and Bethe-Salpeter Equation calculations were used to evaluate their optical properties.

4.1 Lattice Parameters

The first step in most ground state calculations is the determination of the most stable atom configuration, and since we are dealing with periodic structures the lattice parameters are what we are looking for.

In the introduction, the structure of these materials was mentioned briefly but for completeness of this Chapter they will be mentioned again in more detail.

All of the ZnX materials crystallize in the Zinc-Blende (ZB) structure (also known as sphalerite), space group: $F\bar{4}3m$, Number: 216, which is basically the diamond structure with Zn at the (0,0,0) and X at the (0.25, 0.25, 0.25) positions. They can also be found in the wurzite structure which is hexagonal, space group: $P6_3mc$, Number:186. In both structures the chalcogen atoms form tetrahedra with Zn atoms inside. The primitive cell of the two structures can be seen in Fig.4.1 while the atom positions and basis vectors for both structures can be seen in Table A.1 of Appendix A. All of the ZnX materials favour the ZB structure.

To find the lattice parameters, DFT is employed to calculate the ground state energy of

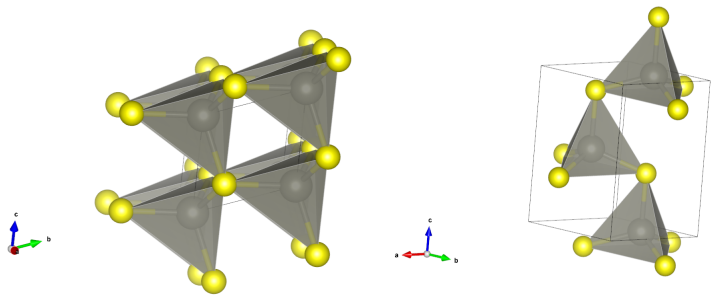

Figure 4.1: The primitive cells of the two structures of the Zn chalcogenides. The chalcogen atoms are depicted yellow and Zn is grey. Left: The ZB structure, Right: The wurtzite structure.

different atom configurations. The configuration with the minimum energy is the most energetically favoured and the one we are looking for.

In the case of the ZB structure there is only one lattice parameter: a. After an initial investigation with broader lattice parameter screening we performed a narrower search to find the most energetically favoured value. The lattice constants were found to be 5.45 Å 5.74 Å and 6.18 Å for ZnS, ZnSe and ZnTe, respectively.

Table 4.1: Experimental data for the ZnX series for the lattice parameter and the Energy-Band gaps.

	a (Å)	$Eg_{optical}$(eV)
ZnS	5.406 [22]	3.73 (300^{o}K)[23], 3.66(300^{o}K)[24]
ZnSe	5.667 [22]	2.81 (20^o K)[25]
ZnTe	6.1026 [22]	2.26(300^o K) [23] , 2.37(4^o K) [26]

The values are in good agreement with experimental data with less than 1.5% deviation from their respective experimental values in Table 4.1. The energy versus lattice parameter graphs can be seen in Fig.4.2 and 4.3.

The computational parameters used in the above calculations could be considered accurate but the matter of how accurate has yet to be determined. To do this a set of convergence runs were conducted for the Plane Wave (PW) cutoff-energy (ENCUT), number of bands (NBANDS) and k-point grid for ZnS. The results can be seen in Table 4.2.

For a 6x6x6 k-point grid the energy is already converged to 0.002eV, 100 bands are already converged to 0.00001eV and for 600eV PW ENCUT the calculation is converged to 0.0001eV. A lot of the bands are empty (in this case *empty bands* = NBANDS − 9) but it is a good practice to include some in the calculation and it doesn't do much to worsen the computational load. Table 4.2 can be used to pick the parameters in such a way to achieve the desired computational accuracy.

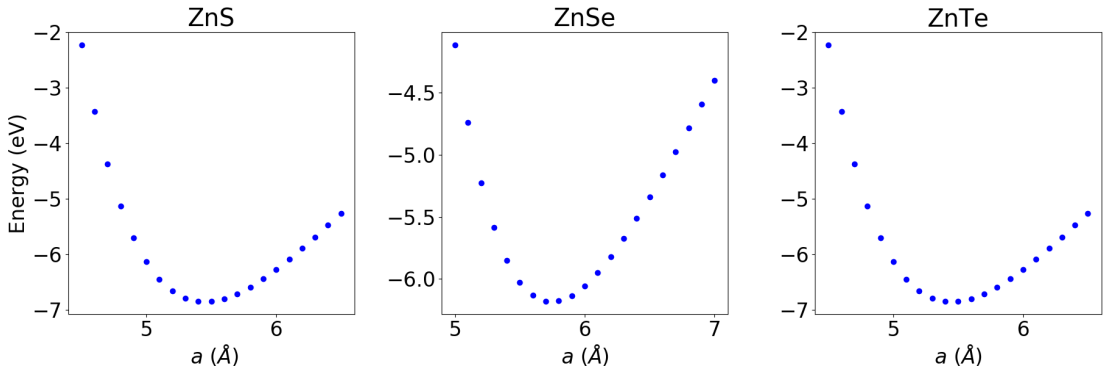

Figure 4.2: Initial screening of the the Energy-Lattice parameter graphs for the ZB structure of the three materials. A 10x10x10 k-point grid was used with 1100eV cutoff energy.

Table 4.2: Convergence investigation for ZnS. Except in the calculations that varied these quantities 200 bands, 700eV PW ENCUT and a 10x10x10 k-point grid were used.

NBANDS	Energy(eV)	Kpt-grid	Energy(eV)	ENCUT	Energy(eV)
100	-6.8512960	6x6x6	-6.8482654	200	-6.3992828
150	-6.8512869	8x8x8	-6.8510391	400	-6.8500525
200	-6.8512865	10x10x10	-6.8512865	600	-6.8513130
250	-6.8512867	12x12x12	-6.8513201	700	-6.8512865
		14x14x14	-6.8513256	1100	-6.8513244

Additionally, we performed ground-state calculations of the wurtzite structure of these materials in order to confirm that the cubic ZB is the most stable at lower temperatures (in all our calculations we have 0 Kelvin). Their lattice constants were found by minimizing the energy versus the three lattice parameters a, c and u (u is a parameter that affects the chalcogen positions) using the Nelder-Mead (simplex) optimization algorithm. The results of this investigation can be found in Table 4.3.

As can be seen in table 4.3, there is small difference in energies per atom, as expected, as both can be synthesized easily and can be found in nature. There is a trend showing that the Zinc-Blende structure is more favourable as the chalcogen atom gets heavier.

4.2 Electronic Properties

4.2.1 Bandstructures

The bandstructures of these materials were also calculated and can be seen in Fig.4.4. We confirm the well-known direct gap at the Γ point of the Brilluin Zone of these materials that gives rise to their optoelectronic properties but the DFT band gaps are,

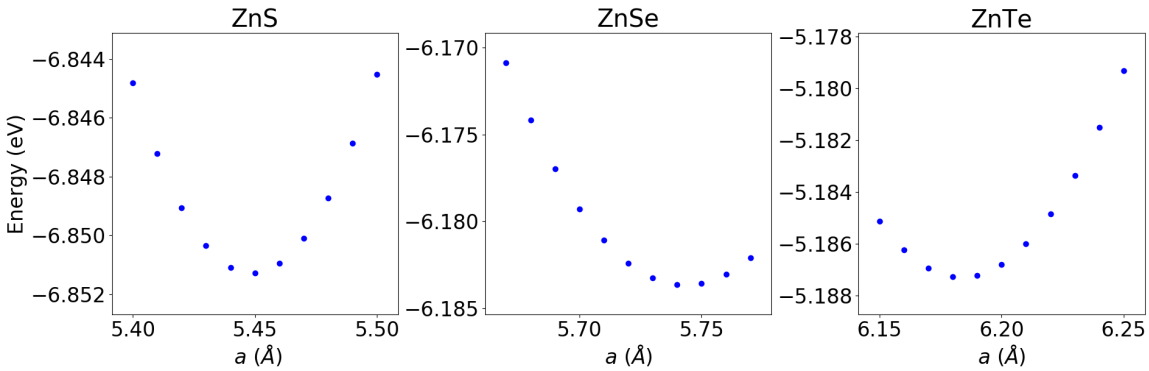

Figure 4.3: The Energy-Lattice parameter graphs for the ZB structure of the three materials in the minimum neighbourhood. A 10x10x10 k-point grid was used with 1100eV cutoff energy.

Table 4.3: Lattice Parameters for the two structures of the ZnX materials. All energies and energy differences are in eV.

Parameter	ZnS		ZnSe		ZnTe	
	Wurzite	ZB	Wurtzite	ZB	Wurtzite	ZB
a (A)	3.85	5.45	4.04	5.74	4.35	6.18
c (A)	6.31	-	6.60	-	7.16	-
u	0.374	-	0.375	-	0.374	-
Energy/atom	-3,4229	-3.4257	-3.0861	-3.0919	-2.5874	-2.5937
Energy Difference	0.0028		0.0058		0.0063	

as expected, greatly underestimated. This is a well-known weakness of DFT as it is not suitable for excited states and does not perform well when calculating the electron addition and extraction energies.

The direct transition at Γ corresponds to the first exciton while the one at Λ to the second exciton. The band-gaps in the graphs are: $\approx$ 2.0 eV, 1.2 eV and 1.1 eV for ZnS, ZnSe and ZnTe, respectively. The DFT bands gaps can be found also in Table 4.5. The bandstructures display other similar features too, like the behaviour of the first three valence bands, they share similar gradients at the same k-points and hence hole effective masses too and they all degenerate to one energy at the Gamma point. We remind at this point that the effective mass of an electron/hole is inversely proportional to the gradient of the energy in k space. There are also the almost flat bands at ≈ -7 eV that can be attributed to localized d states because of the extremely large mass of the electrons there. The aforementioned features are also present in the more accurate bandstructure calculated for ZnS and ZnSe in the GWA by Weidong Luo *et al.* [27] with the addition of a band-gap much closer to the experimental values.

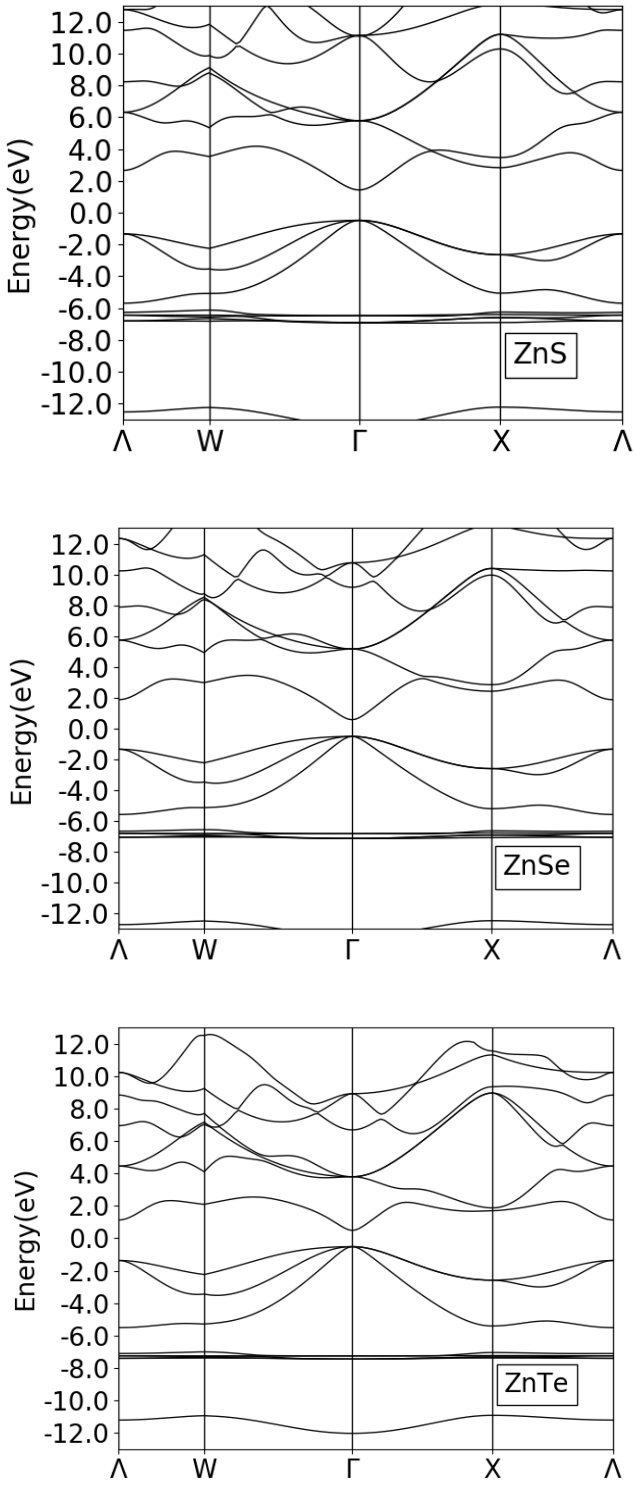

Figure 4.4: Bandstructures of the ZnX materials. PW ENCUT was 1200eV and 40 kpoints in each line were considered.

4.3 GWA and BSE calculations

For the GW calculations there were a number of parameters to check out for convergence and the results of the calculations will be presented in the following tables. In most of these calculations, the G_0W_0 approximation was used except the one about the number of iterations whose the GW_0 approximations was used when more than iteration was used.

Table 4.4: Convergence calculations for ZnS. Other calculations parameters until otherwise mentioned: ENCUT = 600 eV, NBANDS = 248, NBANDSV = 12, kpoint-grid = 4x4x4 , ENCUTGW = 400eV, NBANDS = 50

G Iterations	Eg_{DFT}	Eg_{GW0}	ENCUTGW	Eg_{DFT}	Eg_{G0W0}
1	1,9931	3,3561	150	1,9931	3,3954
3	1,9931	3,6227	200	1,9931	3,3708
5	1,9931	3,6336	300	1,9931	3,3520
7	1,9931	3,6342	400	1,9931	3,3562
NBANDS	Eg_{DFT}	Eg_{G0W0}	ENCUT	Eg_{DFT}	Eg_{G0W0}
150	1,9931	3,3485	300	1,9869	3,3481
200	1,9931	3,3524	400	1,9912	3,3554
248	1,9931	3,3562	600	1,9931	3,3561
NBANDSV	Eg_{DFT}	Eg_{G0W0}	NOMEGA	Eg_{DFT}	Eg_{G0W0}
9	1,9931	3,3561	30	1,9931	3,3588
12	1,9931	3,3561	50	1,9931	3,3561
18	1,9931	3,3562	70	1,9931	3,3596

In Table 4.4 the effect of the GWA flavour can already be seen. With just three iterations the prediction for the band gap dramatically improves and the energy is converged to 0.01eV. ENCUTGW is converged to 0.001eV for 300eV while NOMEGA and NBANDSV seemed well converged for all tested values and it would not be wise to lower these parameters further since they don't affect the computational time that much. The only non-GW parameters are the NBANDS and ENCUT for which both the DFT and GWA band-gap are converged to 0.001eV for 150 bands and 400eV. We performed more convergence calculations for ZnS and the other two materials as well that can be found in Tables A.2, A.3 and A.4 of Appendix A.

We then went on to calculate the electronic band gaps for the whole ZnX family using three different approaches for the GWA. The calculated gaps can be found in table 4.5.

As can be seen from Table 4.5 DFT gap energies are well converged even for a 4x4x4 k-grid while the GW calculations require denser k-point sampling still to reach that level of accuracy, they are converged to 0.01 eV though when using a 6x6x6 grid. Unfortunately, these calculations require tremendous memory, making further investigation

Table 4.5: Band Gaps (in eV) of the materials as calculated by different flavors of GW approximation.

Material(k mesh)	a (Å)	Eg (DFT)	Eg (G0W0)	Eg (GW0)	Eg (QPGW0)
ZnS (4x4x4)	5.45	1.99	3.35	3.62	3.65
ZnS (6x6x6)	5.45	2.00	3.27	3.52	3.57
ZnS (8x8x8)	5.45	2.00	3.26	3.51	3.56
ZnSe (4x4x4)	5.74	1.16	2.43	2.67	2.80
ZnSe (6x6x6)	5.74	1.17	2.34	2.55	2.71
ZnTe (4x4x4)	6.18	1.06	1.92	2.08	2.12
ZnTe (6x6x6)	6.18	1.07	1.84	1.98	2.04

difficult, but a great improvement can be observed when using the GW_0 method, that updates the DFT eigenenergies. Moreover, as we increase the k-point sampling the energy tends to decrease. Still, the agreement with the experiment in the GW_0 and the $QPGW_0$ approximations is remarkable with $\approx 10\%$ deviation for ZnTe and a much better agreement for ZnS and ZnSe with their respective band gaps being just $\approx$ 1-5% off.

In the literature there is a tendency of the $QPGW_0$ to overestimate the gap and the results of GW_0 are considered more credible even though it is not updating the one-electron orbitals in its self-consistency scheme. This is attributed to error cancellation with the negligence of the vertex corrections.

The work of Riefer *et al* [28] is very similar to ours in which they studied the same materials. They used DFT in the PAW implementation of VASP but for their ground state calculations they used a hybrid DFT method (HSE) which they used as a base for their GWA calculations and they, too, tried different GWA flavours. They were able to use much denser k-point grids, reaching as high as 18x18x18. In their results all the band gaps calculated with the GWA were overestimated with the ones closer to the experiment being with the simple G_0W_0 method. Khidzir *et al* [29] studied ZnSe in the GWA on LDA and found a gap of 1.971eV and had also gathered a lot of other values found in the literature and it seems there is a great range of band gap values from the GWA ,from their work with 1.971 eV to 3.26 eV.

4.3.1 Optical Spectra

After the GWA calculations we performed the BSE calculations to get the optical spectra. Optical spectra can be also calculated in both the DFT and GWA levels of theory but the calculated excitation energies are not that close to the experimental values usually. We remind at this point that the polarizability of the GWA matches the one from the random phase approximation (RPA). In the GWA calculations of the gap the importance of a dense k-point grid was highlighted so we started by calculating the absorption spectra of ZnS for various k-point grids for the three levels of theory(DFT, GWA-RPA, BSE)

in G_0W_0 approximation. As mentioned in Chapter 3, BSE is used on a preceding GWA calculation so the energies in BSE differ depending on the type of GWA that it was based on. The absorption of a material is described by the imaginary part of the dielectric function so this was the quantity we calculated.

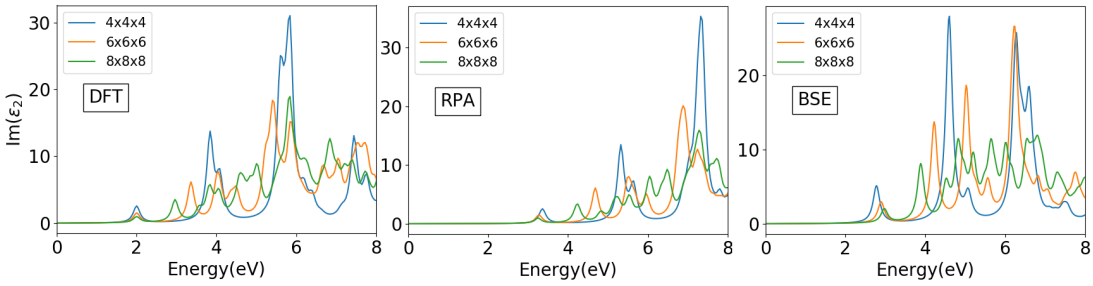

Figure 4.5: Effect of the k-point mesh for three levels of theory of the calculated imaginary part of the dielectric function of ZnS. GWA was used in the G_0W_0 type.

The effect of the k-point grid in Fig.4.5 is quite prominent in all levels of theory. The most notable effect is the appearance of more peaks in all levels of theory. This makes perfect sense because only direct transitions are allowed so denser grid sampling means more optical transitions. In the DFT level the positions of the peaks of lower grid-sizes does not change at all at higher grid-sizes, there is just the emergence of new peaks, meaning the peak positions are converged. The same cannot be said for the other two levels of theory, where the 1st peak position isn't adequately converged for the 4x4x4 grid and is converged to 0.1eV for the 6x6x6 grid while the effect is somewhat more pronounced for transitions at higher energies. Unfortunately, using denser k-point grid sampling was prohibitive due to the computational cost, especially the memory requirements. Even for the 8x8x8 k-point grid, BSE calculations on the other two materials of the series were stopped because they exceeded the computational capabilities of our system. Another common feature of the three levels is the diminishing ε_2 values on the whole spectrum.

The effect of the GWA approximation used was also explored. Calculations using the G_0W_0, the GW_0 and the GW_0 types of GWA were performed on ZnS, the results of which can be seen in Fig.4.6.

The DFT spectra were not shown in Fig.4.6 because they naturally weren't affected. It seems the type of GWA that was considered only affects the quasiparicle energies, hence the peak positions too and slightly ε_2 values. The same effect is also reflected in the BSE spectra which indeed makes sense because the BSE calculation uses the eigenvalues from the GWA.

Even though we weren't able to achieve the level of accuracy intended we proceeded to calculate the optical spectra for the other two materials of the ZnX family for the three theory levels using the $QPGW_0$ since in our study seems to provide the most accurate

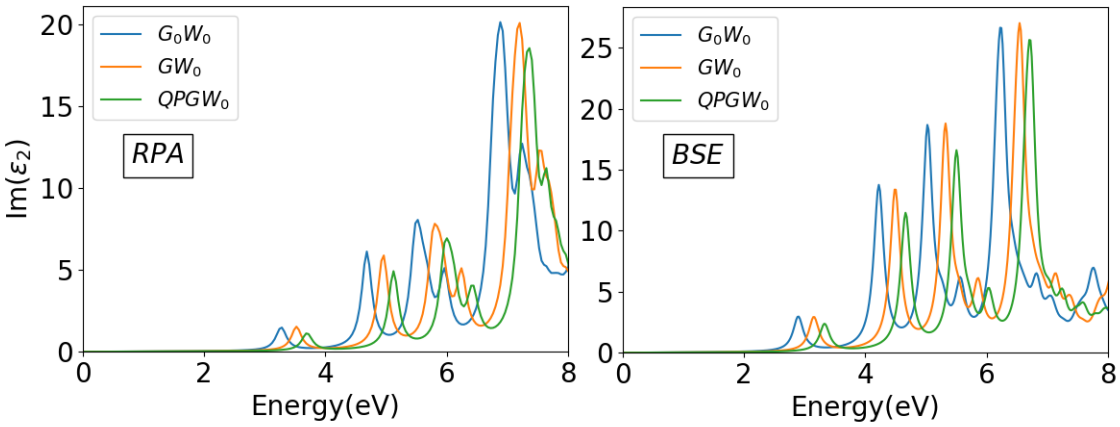

Figure 4.6: Effect of the GWA flavour on the imaginary part of dielectric function calculations for ZnS. For these graphs a 6x6x6 kpoint grid was used.

results among the methods used. A 6x6x6 k-point grid was used.

According to our results in Fig.4.7 the most accurate spectra in terms of the first excitation energy are in the RPA and not in the BSE. This is somewhat surprising since in the RPA excitonic effects are neglected but on the other hand the materials under investigation are in their bulk form and the exciton binding energies are quenched. According to magnetoreflectance studies in the literature the binding energy of the first exciton of ZnSe is 17.4 meV[30] while photoluminescence spectra of ZnTe indicate an exciton binding energy of 12.7 eV [31]. These exciton binding energies exceed the accuracy of our calculations due to the sparse k-point grid. If we take the binding energy of an exciton to be the difference between the GWA electronic gap and the first peak of the BSE spectra our calculations give strongly bound excitons of the order of $\approx$ 100meV.

In Fig. 4.8 the spectra of the whole ZnX family can be seen. The first optical excitation peak lowers in energy as the chalcogen atom gets heavier following of course the trend of the band gaps. This is also reflected on the natural colours of these materials. ZnS having a large band gap, higher in energy than visible light appears in a white hue as it reflects most of the light back, ZnSe has a lower gap and appears yellow because it absorbs all light bellow yellow and ZnTe with a considerably lower band gap appears dark brown as it absorbs more wavelengths. The optical absorption spectrum of ZnSe is really similar to ZnS but ZnTe seems quite different, for example the second and third optical transition of ZnTe seem much closer in energy than the respective peaks of ZnS and ZnTe.

We believe that for a denser k-point grid, absorption spectra closer to the experimental can be achieved. In the literature Riefer *et al* [28] were able to adequately reproduce the optical spectra of the ZnX materials with BSE on G_0W_0 calculations and a 18x18x18 k-point grid and 0.2 eV broadening of the spectral peaks.

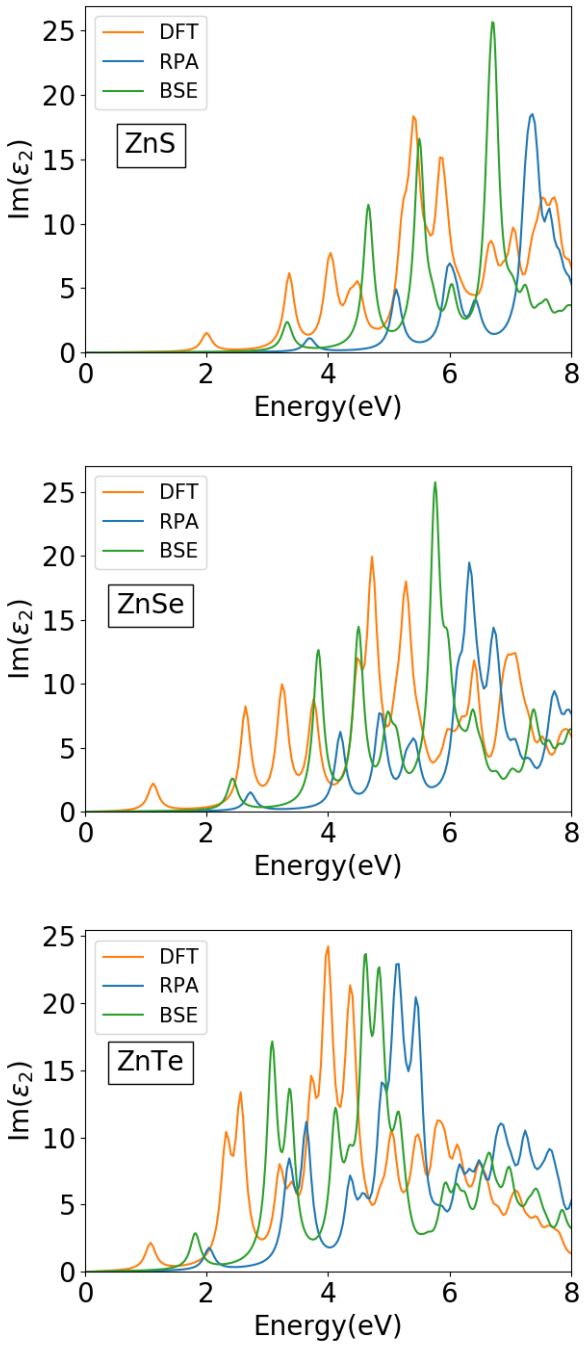

Figure 4.7: The optical spectra for the ZnX family in the three theory levels using the QPGW0 approximation.

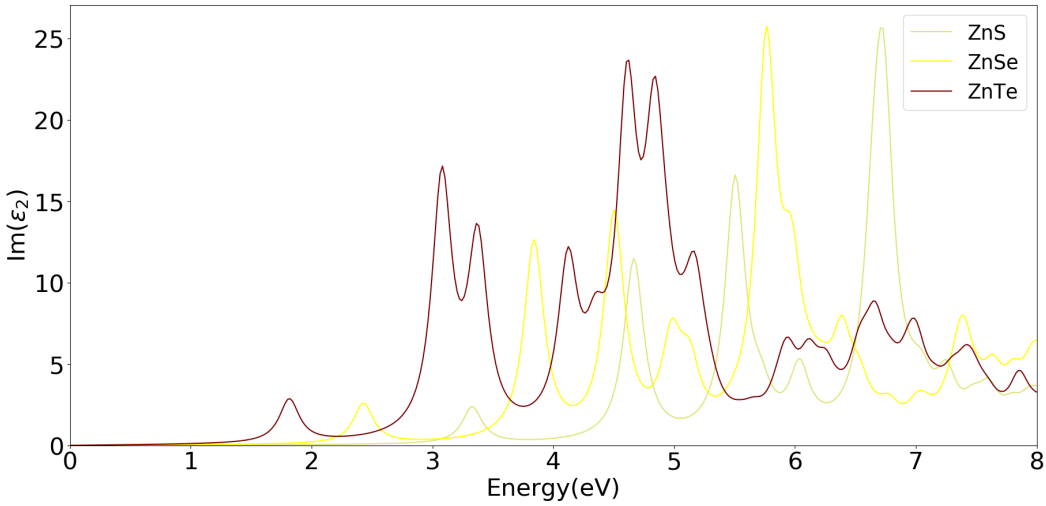

Figure 4.8: The BSE absorption spectra for the ZnX family grouped up. These spectra are based on the QPGW0 approximation on a 6x6x6 k-point grid.

CHAPTER 5

Complex Zn Materials

In this chapter some complex Zn containing materials will be explored. The materials in question belong in two series that experimental colleagues of ours have been studying as temperature sensors, $Mn_{2.5-x}Zn_xNi_{0.5}O_4$ and $Mn_{2.5-x}Zn_{0.5}Ni_xO_4$ for 6 different x values each. In the first, they started with $Mn_{2.5}Ni_{0.5}O_4$ and went on to replace Mn atoms with Zn, while in the latter they started with $Mn_{2.5}Zn_{0.5}O_4$ and the rest of the series have Mn atoms replaced by Ni.

These materials , to the best of our knowledge, haven't been studied before, so in order to get a better grasp of the problem, some preliminary calculations were performed in two similar and well-studied materials. These materials are known to have magnetic orderings so for all the calculations of this chapter included also the spin of each atom. We provide an initial guess of magnetic moments and VASP relaxed them to find the minimum of the energy.

5.1 Mn_3O_4 and Mn_2NiO_4

The crystal structures of these materials are quite similar, Mn_3O_4 crystallizes in the Hausmannite structure [32] ($spacegroup : I4_1/amd, Number : 141$) which is a tetragonal distortion of the cubic spinel structure($spacegroup : Fd\bar{3}m, Number : 227$). Mn_2NiO_4 can be found in the inverse spinel structure but is not always completely inversed[33]. In this study we considered only the normal spinel for Mn_2NiO_4. The primitive cells and atom positions can be found in Table B.1 of Appendix B. We used these primitive cells to construct various supercells in order to have more options for the doping concentration.

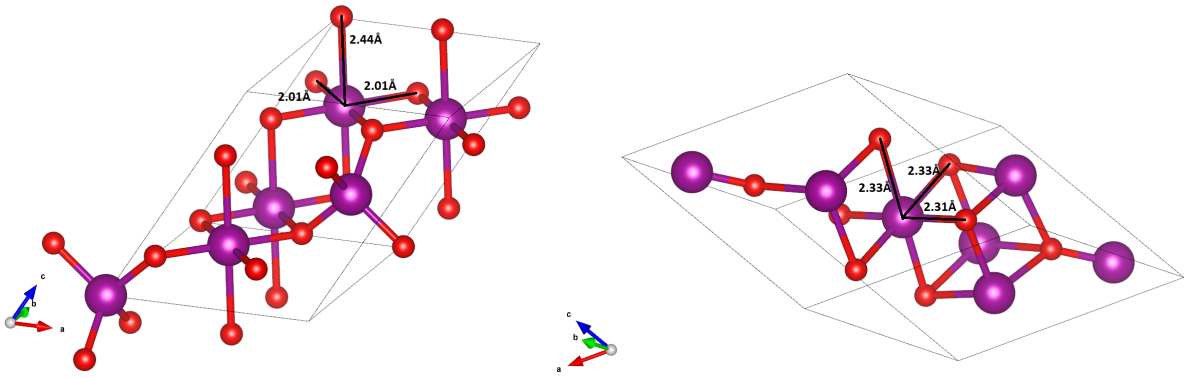

Figure 5.1: Left: The hausmannite primitive cell of Mn_3O_4 and the most stable one. Right: The spinel primitive cell of the same material. The Jahn-Teller effect of Mn_3O_4 distorts the octahedra and lowers the energy.

The distortion in the Hausmannite takes place in the octahedra of the structure in which one of the axis becomes elongated thanks to the Jahn-Teller effect. The Jahn-Teller effects dictates that for a non-linear system, if two orbitals are spatially degenerate they will distort to lift the degeneracy, breaking symmetry in the process, in order to reach a more energetically favoured state.

In both structures the metal ions are located in tetrahedral (A) sites, and twice as many octahedral(B) sites, with O atoms at the vertices. In the case of Hausmannite Mn^{2+} and Mn^{3+} occupy the A and B sites respectively while for the spinel Mn_2NiO_4, Ni^{2+} is at the A and Mn^{3+} is in the B site.

The difference between the normal and the inverse spinel is that the A site atoms are switched with half of the B sites, so in the case of Mn_2NiO_4, the B sites would be occupied by half Ni - half Mn atoms and the A sites by Mn.

Both their primitive cells contain 14 atoms, or 2 formula units(fu), with 6 metal ions and 8 O atoms, The two structures can be seen in Figure 5.1.

5.1.1 Ground state properties of Mn_3O_4

We used the experimental atom positions for the primitive cell provided by [32] as a starting point. The ground state magnetization of this material undergoes various transitions [34] and many theoretical groups have studied this material and find it to be in the anti-ferromagnetic state [[34],[35],[36]]. We performed our own calculations for some of the possible magnetic configurations and we found out that the most stable one is the anti-ferromagnetic as well. This is in contrast with the other spinels that showcase strong anti-ferromagnetic coupling between the A and B sites making them ferrimagnetic. Our results can be seen in Table 5.1.

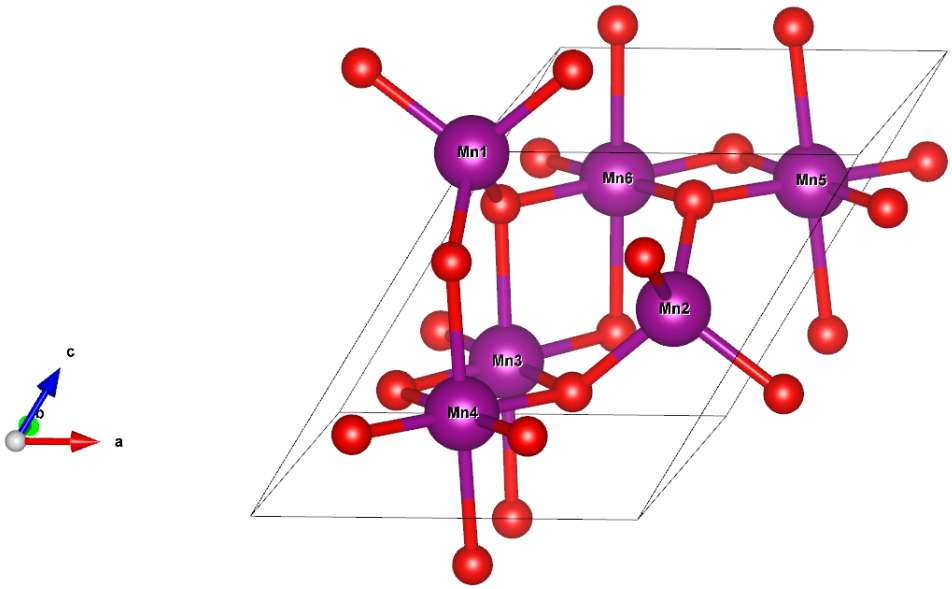

Figure 5.2: Primitive cell of Hausmannite Mn_3O_4 with the atoms labels used for Table 5.1 shown. The primitive cell contains 2 formula units. Mn atoms are depicted purple and O atoms red. Mn1 and Mn2 form tetrahedra with their surrounding oxygen atoms while the rest octahedra.

Table 5.1: Ground State Energy for various magnetic configurations of Mn_3O_4. Mn1 and Mn2 atoms are in tetrahedral sites while the rest are in octahedral site. Calculation Parameters: Energy Cutoff=600eV, 200 bands, 9x9x9 k-points grid, the structure was allowed to relax. FeM, A-FeM and FiM stand for ferromagnetic, anti-ferromagnetic and ferrimagnetic.

Spin Ordering	Mn1(A)	Mn2(A)	Mn3(B)	Mn4(B)	Mn5(B)	Mn6(B)	Energy(eV)
FeM	↑	↑	↑	↑	↑	↑	-115,72
A-FeM	↑	↓	↑	↑	↓	↓	-116.44
A-FeM 2	↑	↓	↑	↓	↑	↓	**-116.70**
FiM	↑	↑	↓	↓	↓	↓	-116.60

In the above calculation the cell volume was allowed to relax while keeping the fractional positions of the atoms fixed in order to get the most stable cell.

According to [37] the experimental values are a= 5.75 Å and $c = 9.42$ Å respectively but if it is to be compared with the spinel cube, a pseudo-cell of this structure has the parameters $a' = a * \sqrt{2} = 8.14$ Å and $c' = c = 9.42$ Å with a $\frac{c'}{a'} = 1.157$ Å. In our calculations the lattice parameters for the energetically favoured anti-ferromagnetic spin ordering were found to be: a = 5.71 Å and c=9.84Å with a $\frac{c'}{a'} = 1.21$

Lastly we performed a spin-resolved DOS calculations for the antiferromagnetic Mn_3O_4. The results of this calculation can be seen in Fig. 5.3

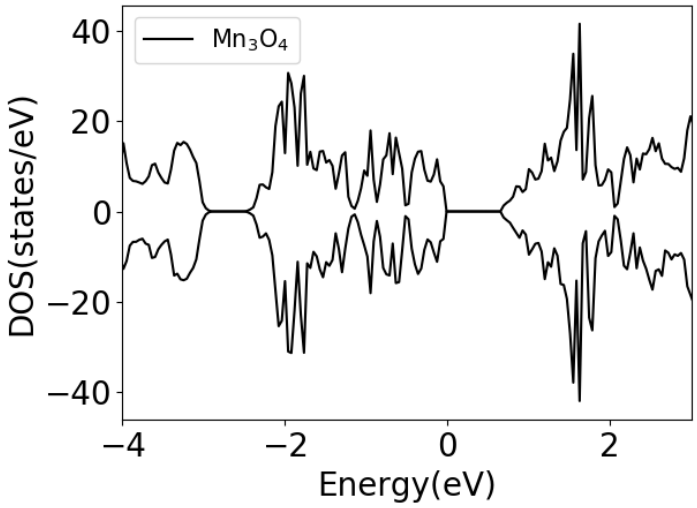

Figure 5.3: The spin-resolved density of states of the Hausmannite Mn_3O_4. Negative values imply spin-down states. Computational Parameters: PW ENCUT = 500 eV, NBANDS = 250, 5x5x5 k-point grid. This calculation was performed on a 2x1x1 supercell of the primitive cell.

Our results for the hausmannite show a band gap of around 0.7eV which is far from the experimental value of 2.6eV which is to be expected as discussed in the previous chapter too, but our gap is in close agreement with the results obtained by theoretical groups like [35].

5.1.2 Mn_2NiO_4

For the spinel Mn_2NiO_4 we started again by finding the lattice parameters and the ground state magnetization using the simplex algorithm. We used a supercell containing 8 formula units (4 primitive cells or 56 atoms in order to have more options later for the doping percentages) and found its lattice parameter to be a=8.35Å and the oxygen

parameter x=0.384 Å. These values are in close agreement with the values given for the inverse spinel by [37] that gives the experimental values: a=8.40Å and x=0.3835.

As mentioned in the beginning of section 5.1.1, spinel materials are usually ferrimagnetic having opposite magnetic moments for the tetrahedral and octahedral sites of the lattice and it is for this ordering that we found the lattice parameters. We wanted to make sure that this is the ground state magnetization so we performed some extra tests, even for random initial magnetizations for each atom. For the random magnetization we used the 14 atom primitive cell. After the magnetic moment relaxation the most stable spin configuration was the ferrimagnetic one with the magnetic moments of the octahedral (B) sites being opposite to the magnetic moments of the A sites while all the atoms of the same site being parallel . The results can be seen in Table 5.2 while the results for the random initial magnetic moments didn't yield any more favourable configurations and some are presented in Table B.2 of Appendix B.

Table 5.2: Ground state magnetization investigation for the 56 atom supercell of Mn_4NiO_4. In each atom column the number of atoms and the magnetic moments are given for each spin, both their initials values tried and after the relaxation. All magnetic moments are given in μ_B.

Initial Guesses						Relaxed State						Energy(eV)
Mn		Ni		O		Mn		Ni		O		
Up	Down	Up	Down	Up	Down	Up	Down	Up	Down	Up	Down	
16*3	0	0	8*4	16*0.5	16*0.5	16*3.52	0	0	8*1.2	0	32*0.04	-425.73
16*3	0	8*1	0	16*0.5	16*0.5	16*3.52	0	0	8*1.2	0	32*0.04	-425.73
16*3	0	8*6	0	32*0.5	0	16*3.52	0	0	8*1.2	0	32*0.04	-425.73
0	16*0.5	4*1	4*1	32*0.5	0	0	16*3.52	8*1.2	0	32*0.04	0	-425.73
0	16*3	8*4.0	0	16*0.5	16*0.5	0	16*3.52	8*1.2	0	32*0.04	0	-425.73
0	16*3	8*6	0	32*0.5	0	0	16*3.52	8*1.2	0	32*0.04	0	-425.73
16*3	0	4*1	4*1	16*0.5	16*0.5	16*3.52	0	0	8*1.2	0	32*0.04	-425.73
0	16*3	8*4.0	0	16*0.5	16*0.5	0	16*3.52	8*1.2	0	32*0.04	0	-425.72
0	16*1	8*2	0	16*0.5	16*0.5	0	16*3.52	8*1.2	0	32*0.04	0	-425.71
8*5	8*5	4*6	4*6	16*0.5	16*0.5	8*3.2	8*3.2	1*1.09	7*0.8	9*0.02	23*0.04	-423.41
8*3	8*3	8*1	0	16*0.5	16*0.5	8*3.2	8*3.2	4*0.5	4*0.15	20*0.01	12*0.1	-423.32
6*3	10*2	2*7	6*4	16*1	16*2	6*3.4	10*3.0	5*0.3	3*3	10*0.01	22*0.02	-423.19
16*0.5	0	4*1	4*1	32*0.5	0	16*3.4	0	4*0.9	4*1.2	16*0.04	16*0.04	-423.1
16*3	0	8*1	0	32*0.5	0	16*3	0	8*0.9	0	32*0.02	0	-420.7
6*5	10*7	2*5	6*3	32*0.5	0	16*3.2	0	7*0.01	1*0.06	17*0.01	15*0.02	-420.07

The convergence of our calculations was examined next and can be seen in Table 5.3. NBANDS again don't affect our calculation much, with 250 the energy is already converged to the 5th decimal digit. For a 5x5x5 k-point grid the energy is converged to 0.005eV but PW ENCUT seems to need 900eV to converge to 0.01eV.

We also calculated the DOS of this material shown in Fig 5.4. The material seems metallic with a spin-down gap near the Fermi energy.

5.2 Zn substitutions in Mn_2NiO_4

We then tried substituting the Mn atoms in the octahedra with Zn. Zn, even though assumed with a magnetic moment at first, after all the following calculations relaxed to a 0 magnetic moment. Using the same 56 atom unit cell we tried 5 different Zn substitutions concentrations 6.25%, 12.5%, 18.75%, 25% and 31.25%. We set up a

Table 5.3: Convergence Table for Mn_2NiO_4. In the cases that they didn't vary the parameters used are: PW ENCUT = 600eV, k-point mesh = 3x3x3 and NBANDS = 250.

k-point mesh	Energy (eV)	NBANDS	Energy (eV)
3x3x3	-425.66679	250	-425.66679
5x5x5	-425.69395	300	-425.66680
7x7x7	-425.69872	350	-425.66681
9x9x9	-425.69922	400	-425.66681

	ENCUT (eV)	Energy (eV)
	500	-425.72462
	600	-425.66679
	700	-425.71157
	800	-425.75508
	900	-425.76864

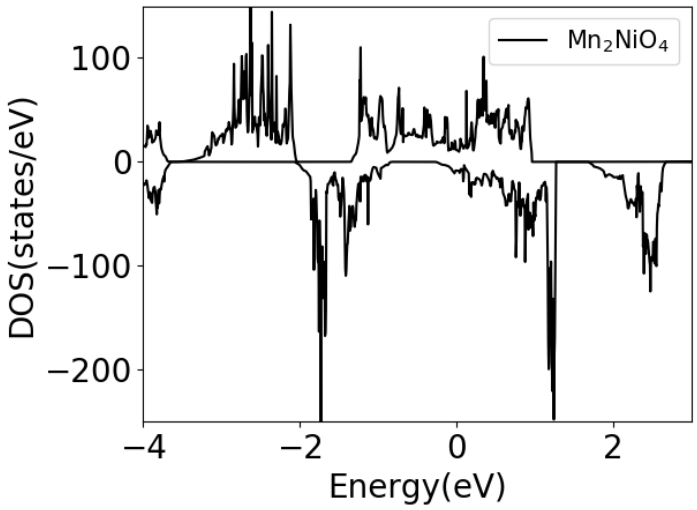

Figure 5.4: The spin-resolved density of states of the spinel Mn_2NiO_4. Negative values imply spin-down states. Computational Parameters: PW ENCUT = 500 eV, NBANDS = 250, 5x5x5 k-point grid.

program to find all the unique configurations of the Zn atoms for all the Zn concentrations and categorized them based on Zn-Zn interactions. In the unit cell used we could find just three unique distances between possible Zn-Zn pairs and named them first neighbour(fn), second neighbour (sn) and third neighbour(tn). Our results are presented in the following tables. In the case of 1 Zn substution there is only one configuration of course. The three possible Zn-Zn interactions can be seen in Fig. 5.5.

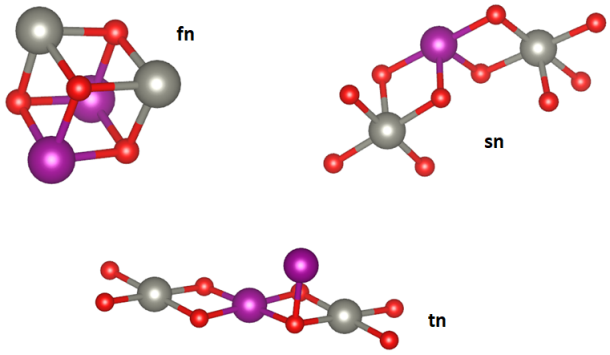

Figure 5.5: The three possible Zn-Zn interactions in the 56 atom supercell of Mn_2NiO_4, namely first neighbour, second neighbour and third neighbour. As neighbours we consider only Zn atoms since it is the only part that changes.

Table 5.4: The number of unique substitution configurations and number of Zn-Zn pairs for various Mn substitution percentages.

Zn substitutions	Mn substitution%	# of unique configurations	# of Zn pairs
0	0.00	1	0
1	6.25	1	0
2	12.50	3	1
3	18.75	8	3
4	25.00	14	6
5	31.25	19	10
6	37.50	16	15
7	43.75	26	21
8	50.00	25	28

All the calculations regarding the Zn substitution in spinel Mn_2NiO_4 were using 500 PW ENCUT, 250 bands, were spin-polarized and let cell volume relax.

As can be seen in Tables 5.5 - 5.8 there is a clear preference of the introduced Zn atoms to stay dispersed and avoid Zn-Zn first neighbour interactions while slightly preferring second over third neighbours. Since we considered the normal spinel, Zn atoms are substituting octahedral Mn which all have parallel magnetic orderings, by dispersing Zn a more uniform magnetization distribution is obtained or else there would be island-like octahedral areas with Mn and a considerable net magnetic moment and other areas

Table 5.5: Possible configurations for 2 Zn atoms introduced.

Zn-Zn interactions	Energy (eV)	Magnetization(μ_B)	Energy Dif.(eV)/unit cell
sn	**-407.9597**	**37.7**	**0.000**
fn	-407.9446	37.7	0.004
tn	-407.7571	37.4	0.050

Table 5.6: Possible configurations for 3 Zn atoms introduced.

Zn-Zn interactions	Energy (eV)	Magnetization (μ_B)	Energy Dif.(eV)/unit cell
0fn, 3sn, 0tn	**-399.0574**	**33.1**	**0.000**
0fn, 2sn, 1tn	-399.0416	33.1	0.004
0fn, 0sn, 3tn	-399.0097	33.1	0.012
1fn, 2sn, 0tn	-398.8479	33.1	0.052
2fn, 1sn, 0tn	-398.6491	33.0	0.102
2fn, 0sn, 1tn	-398.6398	32.9	0.104
3fn, 0sn, 0 tn	-398.3840	32.8	0.168
1fn, 1sn, 1tn			

Table 5.7: Possible configurations for 4 Zn atoms introduced.

Zn-Zn interactions	Energy (eV)	Magnetization (μ_B)	Energy Dif.(eV)/unit cell
0fn, 6sn, 0tn	**-390.1219**	**28.0**	**0.000**
0fn, 4sn, 2tn	-390.0926	28.0	0.007
0fn, 0sn, 6tn	-390.0301	28.1	0.023
1fn, 4sn, 1tn	-389.8974	28.1	0.056
1fn, 2sn, 3tn	-389.8622	28.1	0.065
2fn, 4sn, 0tn	-389.7145	28.1	0.102
2fn, 3sn, 1tn	-389.6949	28.1	0.107
2fn, 1sn, 3tn	-389.6692	28.1	0.113
2fn, 2sn, 2tn	-389.6685	28.1	0.113
3fn, 2sn, tn	-389.4878	28.1	0.159
4fn, 0sn, 2tn	-389.3098	28.0	0.203
4fn, 2sn, 0tn	-389.2545	28.1	0.217
4fn, 1sn, 1tn	-389.2449	28.1	0.219
6fn, 0sn, 0tn	-388.6897	28.0	0.358

Table 5.8: Possible configurations for 5 Zn atoms introduced.

Zn-Zn interactions	Energy (eV)	Magnetization (μ_B)	Energy Dif.(eV)/unit cell
2fn, 7sn, 1tn	**-380.7232**	**23.0**	**0.000**
2fn, 6sn, 2tn	-380.7071	23.0	0.004
2fn, 5sn, 3tn	-380.6773	23.0	0.011
2fn, 4sn, 4tn	-380.6749	23.0	0.012
2fn, 2sn, 6tn	-380.6455	23.0	0.019
3fn, 6sn, 1tn	-380.5154	23.1	0.052
3fn, 5sn, 2tn	-380.5102	23.0	0.053
3fn, 4sn, 3tn	-380.4794	23.1	0.061
3fn, 3sn, 4tn	-380.4655	23.1	0.064
4fn, 4sn, 2tn	-380.3083	23.1	0.104
4fn, 2sn, 4tn	-380.2960	23.1	0.107
4fn, 5sn, 1tn	-380.2647	23.0	0.115
4fn, 3sn, 3tn	-380.2355	23.0	0.122
5fn, 3sn, 2tn	-380.0668	23.1	0.164
5fn, 4sn, 1tn	-380.0659	23.1	0.164
5fn, 2sn, 3tn	-380.0484	23.1	0.169
6fn, 2sn, 2tn	-379.8799	23.1	0.211
6fn, 3sn, 1tn	-379.8175	23.1	0.226
7fn, 2sn, 1tn	-379.5206	23.1	0.301

where Zn atoms are gathered with no magnetic moment. The energy gain seems considerable reaching 300 meV per unit cell or 150meV per f.u. for the most-least favoured configuration for 4 and 5 Zn substitutions. As the doping concentration increases there aren't enough octahedra for Zn atoms to completely avoid each other and already for 31.25% Mn substitution with Zn there are no more configurations without fn-fn Zn-Zn interactions.

As was already mentioned, Zn atoms relaxed to a no-magnetic state and the gradual reduction of the net magnetic moment is obvious going through the different tables.

The density of states for the most stable configurations was also calculated and can be seen in Fig. 5.6 while a version with narrower energy range for Fig. 5.6 is given in 5.7. There are some interesting features in the DOS for the example the spin-down region close the the Fermi level in which the undoped material and for low substitution percentage is conducting still but after 18.75% Mn is substituted there are no more states for the spin-down electrons in the fermi level giving rise to a spin-down gap of $\approx$ 1.2eV. This effect is a feature of a generalized blueshifting of the energies that is particularly noticeable in the regions around -3.5eV, 0eV and 1eV. Another noticeable change is the emergence of new states (or a band) for the spin-down electrons in the region -3eV to -2eV for all Zn containing materials that didn't exist in the undoped one. This new band seems to get broader with increasing Zn content. Finally there is also a new band for the

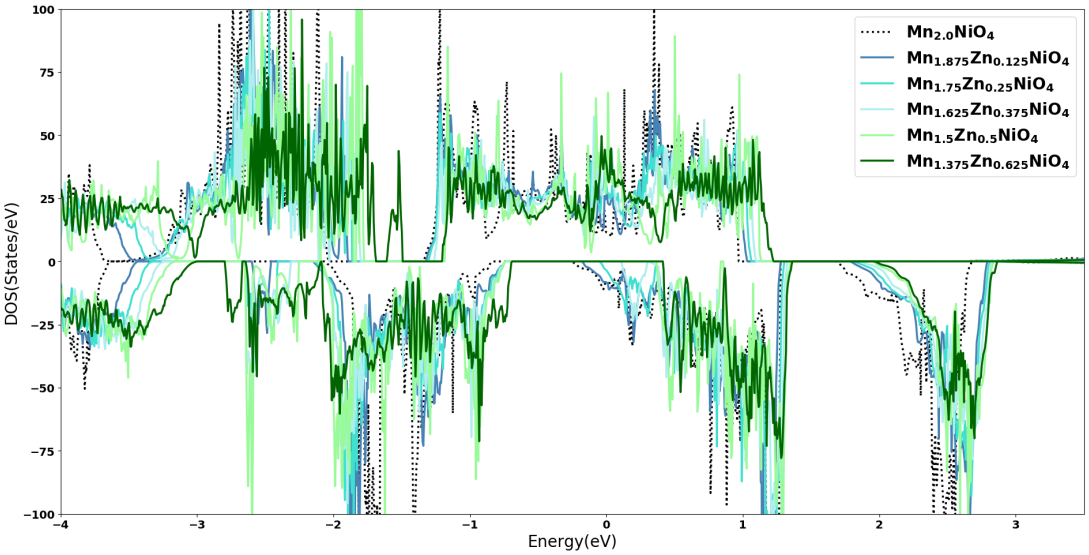

Figure 5.6: Spin-Resolved density of states for the materials with the most stable configuration from each Zn concentration studied and the undoped material.

spin-up electrons at ≈ -1.5eV for the material with the highest Zn concentration.

5.3 The $Mn_{2.5-x}Zn_xNi_{0.5}O_4$ materials

After our initial calculations we proceeded to the materials studied by our experimental colleagues. The first material series consists of $Mn_{2.5}Ni_{0.5}O_4$ and its alloys by Zn substitution , general formula $Mn_{2.5-x}Zn_xNi_{0.5}O_4$ for 5 different x values, 0.25, 0.5, 0.75, 1.0 and 1.25. These materials are quite similar to the Zn-doped Mn_2NiO_4 that were discussed in the previous section but in these materials there are less Ni atoms and hence half the tetrahedral positions are occupied by more Mn.

Initially we investigated whether these materials prefer the Hausmannite, the spinel or the inverse spinel crystal structure. The undoped $Mn_{2.5}Ni_{0.5}O_4$ is a material between the Mn_3O_4 and Mn_2NiO_4 in composition, either as the Ni-doped of the former or the Mn-doped latter. Our calculations indicate that this material, and the rest of the series as well, prefer considerably the hausmannite structure with an energy difference of ≈ 2.5eV per formula unit. We also checked whether the Ni atoms in the un-doped material prefer the tetrahedra (like the normal spinel) or the octahedral (like the inversed spinel) positions and it turns out that the two Ni atoms in the supercell prefer the octahedral positions for ≈ 220 meV. For these calculations we used a 2x1x1 supercell with 900 eV PW ENCUT, 250 bands and a 2x4x4 k-point grid and the cell volume was allowed to relax while keeping the shape of the cell and the fractional positions of the atoms fixed.

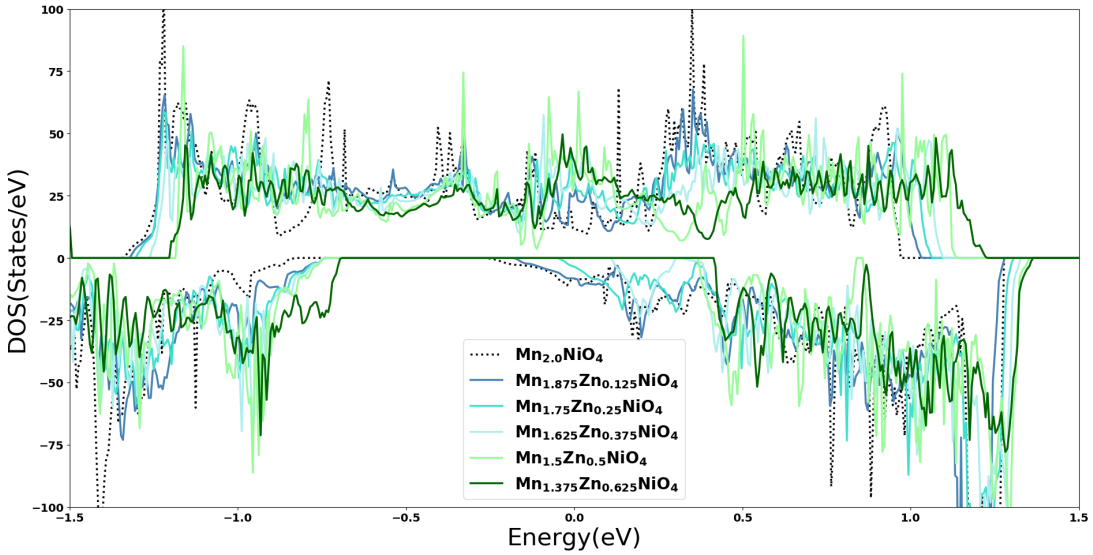

Figure 5.7: Another version of Fig. 5.6 with narrower energy range.

We additionally checked the ground state magnetization and we observed a ferrimagnetic ground state preference for the un-doped material and assumed a similar behaviour from the rest of the series since the un-doped one is closest to Mn_3O_4 that is antiferromagnetic. We performed some convergence runs too for the un-doped case and assumed that the computational requirements for similar level of accuracy. The convergence results can be found in Table 5.9

Table 5.9: Convergence table for $Mn_{2.5}Ni_{0.5}O_4$. Unless varied the parameters that were used were 500 eV PW ENCUT, 250 bands and a 2x4x4 k-point grid.

ENCUT (eV)	Energy (eV)	NBANDS	Energy (eV)	k-point grid	Energy(eV)
500	-220.41886	250	-220.39720	2x4x4	-220.41866
600	-220.45532	300	-220.39720	3x6x6	-220.43499
700	-220.47461	350	-220.39720		
800	-220.50526				
900	-220.50737				
1000	-220.50737				

From here on we decided to use 900 eV ENCUT, 250 bands and a 2x4x4 kpoint grid. We then went on to calculate the formation energies, magnetization and cell volumes of these materials. These data can be found in Table 5.10. The formation energy was calculated using the formula:

$$E_{form} = E_{material} - N_{Mn}E_{Mn} - N_{Ni}E_{Ni} - N_{Zn}E_{Zn} - 8E_{O_2}, \tag{5.1}$$

where N is the number of each atom species in the supercell used and E is the energies found in their stable forms, namely bcc Mn, fcc Ni, hcp Zn and molecular oxygen.

Table 5.10: Formation energies, magnetization and cell volume for the whole $Mn_{2.5-x}Zn_xNi_{0.5}O_4$ series.

Materials	Form. Energy(eV)/atom	Magnetization (μ_B)	Volume(Å^3)
$Mn_{2.50}Ni_{0.50}O_4$	-1.489	18.6	304.70
$Mn_{2.25}Zn_{0.25}Ni_{0.50}O_4$	-1.467	23.1	305.75
$Mn_{2.00}Zn_{0.50}Ni_{0.50}O_4$	-1.446	28.0	306.72
$Mn_{1.75}Zn_{0.75}Ni_{0.50}O_4$	-1.395	23.0	306.29
$Mn_{1.50}Zn_{0.50}Ni_{0.50}O_4$	-1.335	18.1	306.61
$Mn_{1.25}Zn_{1.25}Ni_{0.50}O_4$	-1.283	13.2	307.21

In Table 5.10 the formation energy seems to drop as the Zn doping increases. These structures are all stable since the formation energy is negative, so it is energetically favourable to form these structures. The magnetization follows a more peculiar trend but is easily explained. It increases at first with Zn doping because Zn prefers to replace Mn atoms in tetrahedral sites which are opposite to the overall magnetization and since Zn relaxed to a zero magnetic moment, the overall magnetization increases. From $Mn_{1.75}Zn_{0.75}Ni_{0.50}O_4$ and for higher concentrations Zn has to replace the Mn in the octahedral sites and so the magnetization diminishes. The cell volume on the other hand increases as Zn is larger than Mn until all Mn tetrahedral sites are replaced then drops slightly and begins to slowly increase again but with almost half the rhythm. The drop in the cell volume could be attributed to one less Jahn-Teller stretching of the Zn occupied octahedron.

We also calculated their conductivities which are of the order of 10^3 S/m with two different values for their axes since they are anisotropic in one direction due to the tetragonal distortion of hausmannite. They can be seen in Talbe 5.11. Even though these values are three to four orders of magnitude from conductivities of more common metals it should be noted that these materials are oxides which usually are semiconductors.

Table 5.11: Conductivities for the $Mn_{2.5-x}Zn_xNi_{0.5}O_4$ material series as calculated in the independent particle approximation of DFT. All conductivities are given in Mega Siemens/meter. Indices 1, 2, 3 of the conductivities refer to the main symmetry axis of the materials.

	σ_1 MS m^{-1}	σ_2 MS m^{-1}	σ_3 MS m^{-1}
$Mn_{2.50}Ni_{0.50}O_4$	0.001	0.002	0.002
$Mn_{2.25}Zn_{0.25}Ni_{0.50}O_4$	0.001	0.002	0.001
$Mn_{2.00}Zn_{0.50}Ni_{0.50}O_4$	0.001	0.002	0.001
$Mn_{1.75}Zn_{0.75}Ni_{0.50}O_4$	0.001	0.002	0.001
$Mn_{1.50}Zn_{1.00}Ni_{0.50}O_4$	0.001	0.002	0.000
$Mn_{1.25}Zn_{1.25}Ni_{0.50}O_4$	0.001	0.0026	0.0004

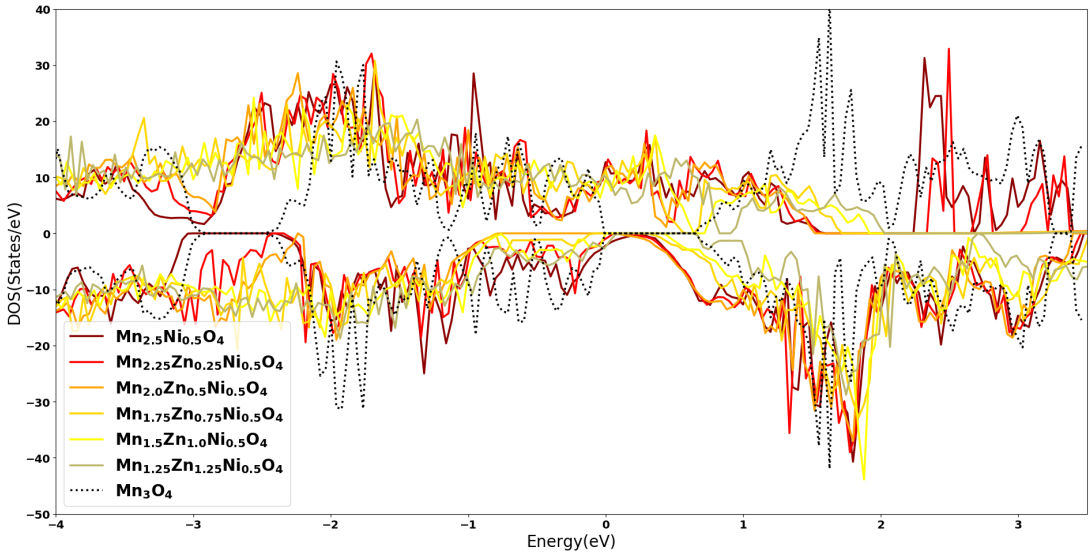

Figure 5.8: The spin-resolved density of states for the whole $Mn_{2.5-x}Zn_xNi_{0.5}O_4$ series and for Mn_3O_4 for reference. Fermi level is set to 0eV. Computational parameters used: 900eV ENCUT, 250 bands and a 2x4x4 k-point grid.

Then we calculated the DOS of these materials which can be seen in Fig. 5.8 and for a narrower energy range version in Fig. 5.9. There are similar features to the ones discussed for the DOS of Zn-doped $Mn_{2.0}NiO_4$. First, there is again the widening of the energy gap of the spin-down electrons near the fermi level which now for higher Zn concentrations seems to have some bands again though. There is again an overall blueshifting that is especially obvious at the spin-down states just below 1eV and the spin-up states at $\approx$ 1.5 eV and of course the new spin down states at $\approx$ 2.5 eV

5.4 $Mn_{2.5-x}Zn_{0.5}Ni_xO_4$

The second materials series we were asked to investigate was $Mn_{2.5-x}Zn_{0.5}O_4$ and its Ni alloys by means of Mn substitution for the same 5 concentrations used in the previous section, one of which is the same ($Mn_{2.0}Zn_{0.5}Ni_{0.5}O_4$).

The structure of the undoped material was expected to be in the hausmannite structure since it is similar to Mn_3O_4 and $Mn_{2.0}ZnO_4$ which both are found in that structure in nature. Our calculations confirmed our expectations for the undoped compound and the rest of the series preferred the Hausmannite over the spinel by $\approx$ 2.5 eV per formula unit. After adding the first Ni atoms we tested which Mn position they prefer to assume and it seems that the first 2 Ni atoms take the tetrahedral sites , by about $\approx$ 250 meV while for higher doping concentrations they are forced to replace octahedral Mn. We continue to use the same computational parameters from the previous series. We calculate again

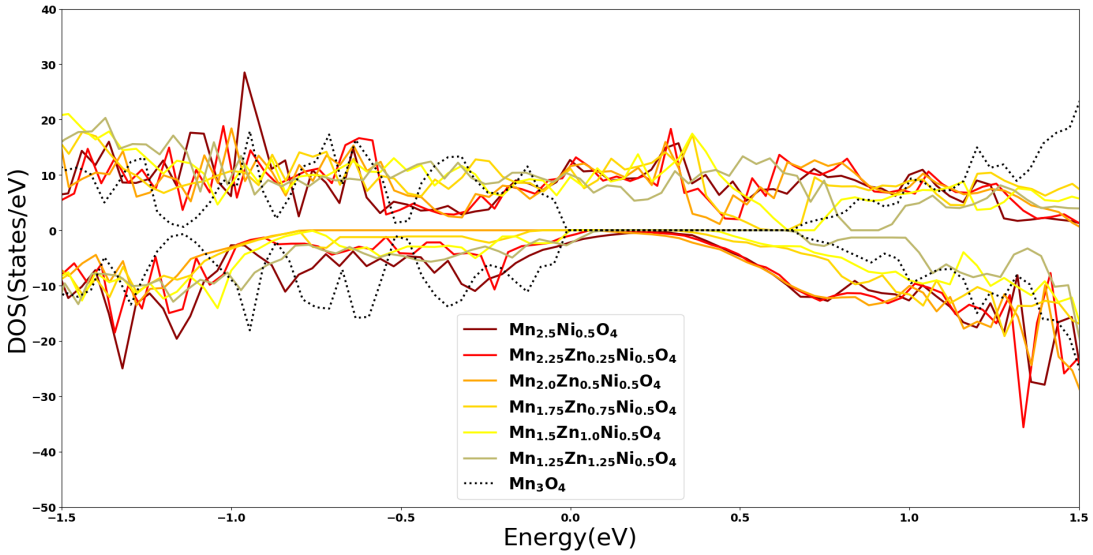

Figure 5.9: Another version of Fig. 5.8 with narrower energy range.

the Formation energies using Eq.(5.1), magnetization and cell volume.

Table 5.12: Formation energies, magnetization and cell volume for the whole $Mn_{2.5-x}Zn_{0.5}Ni_xO_4$ series.

Materials	Form. energy(eV)/atom	Magnetization μ_B	Cell Volume(Å^3)
$Mn_{2.50}Zn_{0.5}O_4$	-1.588	22.3	309.36
$Mn_{2.25}Zn_{0.5}Ni_{0.25}O_4$	-1.518	25.2	308.03
$Mn_{2.00}Zn_{0.5}Ni_{0.50}O_4$	-1.446	28.0	306.72
$Mn_{1.75}Zn_{0.5}Ni_{0.75}O_4$	-1.362	23.0	303.39
$Mn_{1.50}Zn_{0.5}Ni_{1.00}O_4$	-1.282	18.0	300.08
$Mn_{1.25}Zn_{0.5}Ni_{1.25}O_4$	-1.195	13.0	296.91

Once more the formation energies are getting smaller as the Ni doping increases, the magnetization follows the same trend as the previous series and can be explained the same way and finally for this series the cell volume consistently decreases with increasing Ni doping. The trend in the cell volume can be described by the the smaller radius of Ni and again once all Mn in tetrahedra are replaced and Mn in octahedra are replaced the rate that the volume decreases with the concentration can again be explained by less Jahn-Teller stretched octahedra.

The conductivities were calculated for this series as well with an general increasing trend as the Ni content increases. These results can be seen in Table 5.13

The DOS for this series was calculated as well and can be seen in Fig. 5.10 and a narrower energy range version in Fig. 5.11.

Table 5.13: Conductivities for the $Mn_{2.5-x}Zn_{0.50}Ni_xO4$ material series as calculated in the independent particle approximation of DFT. All conductivities are given in Mega Siemens/meter. Indices 1, 2, 3 of the conductivities refer to the main symmetry axis of the materials.

	σ_1 MS m^{-1}	σ_2 MS m^{-1}	σ_3 MS m^{-1}
$Mn_{2.50}Zn_{0.50}O_4$	0.000	0.000	0.000
$Mn_{2.25}Zn_{0.50}Ni_{0.25}O_4$	0.000	0.002	0.000
$Mn_{2.00}Zn_{0.50}Ni_{0.50}O_4$	0.001	0.002	0.001
$Mn_{1.75}Zn_{0.50}Ni_{0.75}O_4$	0.001	0.002	0.002
$Mn_{1.50}Zn_{0.50}Ni_{1.00}O_4$	0.001	0.001	0.004
$Mn_{1.25}Zn_{0.50}Ni_{1.25}O_4$	0.001	0.001	0.004

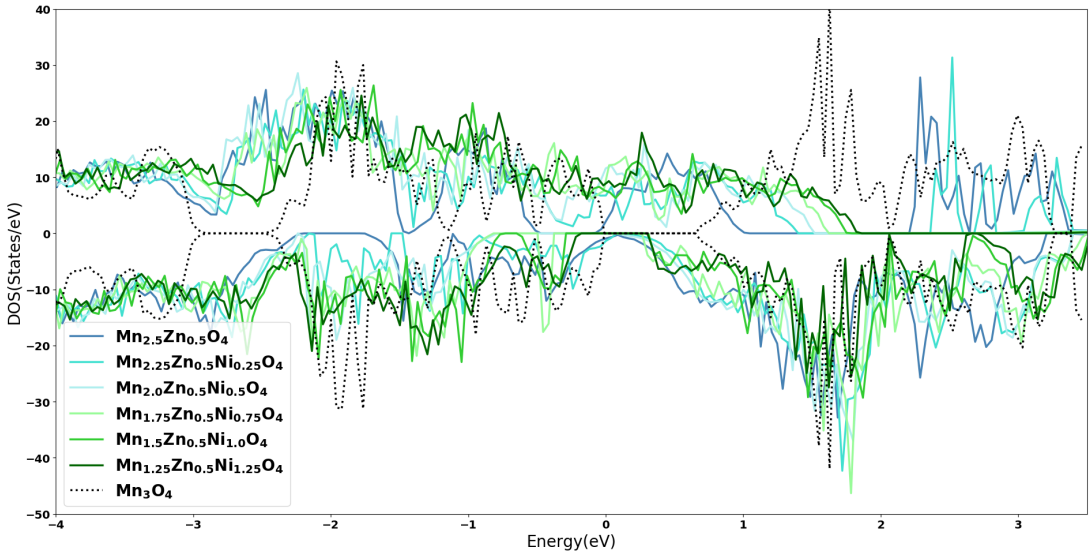

Figure 5.10: The density of states for the whole $Mn_{2.5-x}Zn_{0.5}Ni_xO_4$ series. The fermi level is set to 0.

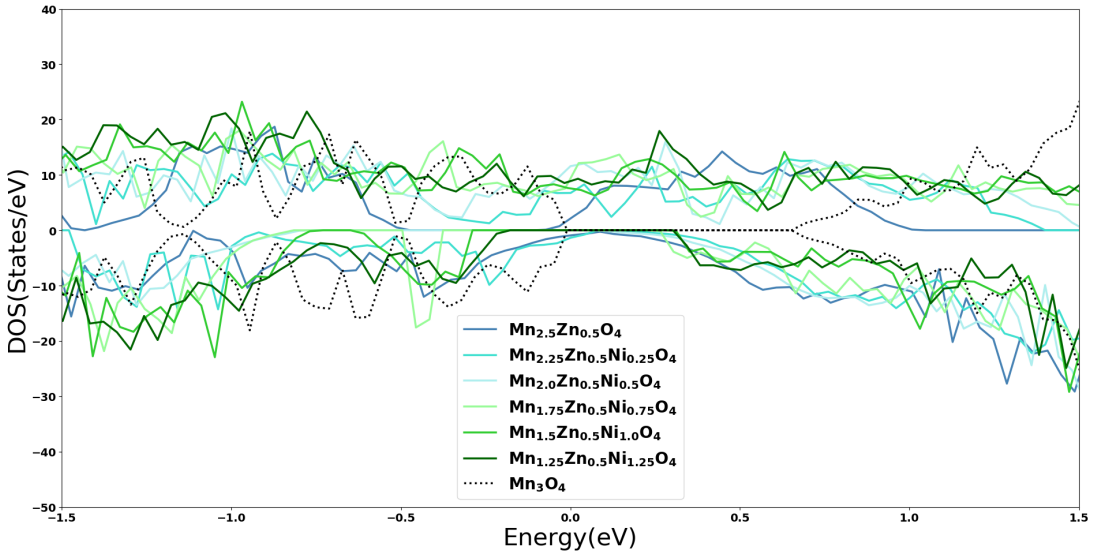

Figure 5.11: Another version of Fig. 5.10 with narrower energy range.

Alloying seems to produce similar effects on all the cases we have studied. We report again the spin-down gap widening close to the fermi level though for this series the fermi level is in the ceter of that gap. There is again the shifting of states to higher energies and the new states emerging at ≈ 2.7 eV.

This half-metallic state has also been reported in the literature by Arras *et al* [34] who studied the spinel Mn_3O_4 and Co_3O_4 and their mixed oxides and even though both these oxides exhibit semi-conducting behaviour but their mixed oxides had spin-up states in the fermi level.

CHAPTER 6

Conclusions and future prospects

In this thesis we used DFT and post-DFT schemes like the GWA and the BSE to calculate the ground-state, electronic and optical properties of two Zn-containing family of materials, the Zn chalcogenides and the Mn-Zn-Ni mixed oxides of the $Mn_xZn_yNi_zO_4$ general type.

In the first part of the thesis we explored the properties of the ZnS, ZnSe and ZnTe. We performed DFT calculations and found among others their lattice parameters, preferred structure, and their bandstructures. We found them all to be in the zinc-blende structure and direct gap semiconductors all in good agreement with the literature except the band gap value that was underestimated, a well-known weakness of DFT. To counter this weakness we employed GWA, in three of its types, and calculated their band gaps, all within 10% error from experimental values. We then solved BSE to get the optical spectra of these materials and compare them with other methods like simple DFT and the GWA (same as RPA) but due to the excessive computational load of GWA and BSE we were unable to converge our calculations to a satisfactory level in terms of the k-point grid and the peak of the first optical transition is better described by the RPA.

For the second part of the thesis we started by studying materials similar to $Mn_xZn_yNi_zO_4$, in particular hausmannite Mn_3O_4 and spinel Mn_2NiO_4. We calculated their density of states and ground state magnetization and found them to be a anti-ferromagnetic semiconductor and ferrimagnetic metal for Mn_3O_4 and Mn_2NiO_4 respectively. We then went on and investigated the effects of Zn-doping by replacing Mn in Mn_2NiO_4 regarding the density of states for all possible configurations of that the Zn atoms can assume for 5 Zn concentrations. We found out that the materials prefer Zn atoms to be dispersed and even with just small concentrations of Zn the density of states changes consider-

ably with a general blueshifting of the energy states, the emergence of new states in the valence band and the transition to half-metallic state. We then proceeded to study the two materials series that our experimental colleagues from FORTH were studying as temperature sensors, $Mn_{2.5-x}Zn_xNi_{0.5}O_4$ and $Mn_{2.5-x}Zn_{0.5}Ni_xO_4$ for 6 x values ranging from 0 to 1.25. According to our results these materials crystallize in the hausmannite structure and seem half-metallic. As the x value increases the effects in the DOS are similar to the Zn-doping in Mn_2NiO_4 we report in the same thesis.

There are still a lot more calculations that can be performed to better understand the materials from the second part of this thesis and along with results from our experimental colleagues we hope to unravel their properties and potential as thermosensors. On our end, there is evidence that implies that the electrons in these materials are strongly correlated and hence the independent particle approximation that is assumed fails. Among others we can study these materials with the DFT+U method to tackle this problem. The Jahn-Teller effect that causes the tetragonal distortion in these lattices is also interesting and its interaction with the substituents requires further investigation.

APPENDIX A

More data from the GW and BSE calculations of the ZnX Series

Table A.1: Atom positions and primitive cells for the ZnX zinc-blende and wurtzite structures. Atom positions are given in fractional coordinates

Zinc-Blende			
		Cell	
A1	a/2	a/2	0
A2	a/2	0	a/2
A3	0	a/2	a/2
Atom Positions (Fract. Coordinates)			
Zn(4a)	0.00	0.00	0.00
X(4c)	0.25	0.25	0.25

Wurtzite			
		Cell	
A1	a/2	$-\frac{1}{2}3^{1/2}$	0
A2	a/2	$+\frac{1}{2}3^{1/2}$	0
A3	0	0	c
Atom Positions (Fract. Coordinates)			
Zn(2b)	1/3	2/3	0
Zn(2b)	2/3	1/3	0.5
X(2b)	1/3	2/3	u
X(2b)	2/3	1/3	(1/2 + u)

Table A.2: All the GW calculations for ZnS. EC stands for the cutoff energy and NBNDS for number of bands. The first peak (and second for the BSE) in the three theory levels and are given. The number after the G in the GW flavor represents the number of iterations of G.

GW flavor	EC	NBANDS	KPOINTS	NBNDSV	EC_GW	NBNDSGW	EgDFT	EgGW	1st DFT p.	1st RPA p.	1st BSE p.	2nd BSE PEAK
QPG3W0	600	500	4x4x4	18	400	50	1.993	3.656	2.002	3.804	3.223	5.085
QPG3W0	800	248	4x4x4	18	400	50	1.993	3.655	2.002	3.804	3.223	5.085
QPG3W0	600	248	4x4x4	18	400	50	1.993	3.655	2.002	3.804	3.223	5.085
QPG3W0	600	248	4x4x4	18	450	50	1.993	3.657	2.002	3.804	3.223	5.085
QPG3W0	600	248	4x4x4	27	400	50	1.993	3.655	2.002	3.804	3.223	5.085
QPG3W0	800	500	4x4x4	18	400	50	1.993	3.657	2.002	3.804	3.223	5.085
QPG3W0	800	248	4x4x4	18	450	50	1.993	3.657	2.002	3.804	3.223	5.085
QPG3W0	800	248	4x4x4	27	450	50	1.993	3.657	2.002	3.804	3.223	5.085
G0W0	600	248	4x4x4	18	400	50	1.993	3.356	2.002	3.363	2.783	4.605
QPG5W0	600	248	4x4x4	18	400	50	1.993	3.666	2.002	3.684	3.083	4.945
QPG3W0	600	248	4x4x4	18	400	100	1.993	3.664	2.002	3.804	3.223	5.085
G0W0	600	248	4x4x4	18	400	50	1.993	3.356	2.002	3.363	2.783	4.605
G0W0	600	248	6x6x6	18	400	50	2.002	3.276	2.002	3.283	2.903	4.224
QPG7W0	600	248	4x4x4	18	400	50	1.993	3.652	2.002	3.644	3.063	4.925
G0W0	600	248	8x8x8	18	400	50	2.003	3.256	2.002	3.243	2.983	3.884
G0W0	600	248	4x4x4	18	400	50	1.993	3.356	2.002	3.363	2.783	4.605
G0W0	600	248	4x4x4	18	400	50	1.993	3.356	2.002	3.363	2.783	4.605
G0W0	600	248	4x4x4	18	400	50	1.993	3.352	2.002	3.363	2.783	4.605
G0W0	600	248	10x10x10	18	400	50	2.003	3.245	2.002	3.243	-	-
QPG3W0	600	248	4x4x4	18	400	50	1.993	3.623	2.002	3.604	3.043	4.905
QPG5W0	600	248	4x4x4	18	400	50	1.993	3.634	2.002	3.644	3.063	4.905
QPG7W0	600	248	4x4x4	18	400	50	1.993	3.634	2.002	3.644	3.063	4.925
G5W0	600	248	8x8x8	18	400	50	2.003	3.508	2.002	3.524	3.223	4.144
G5W0	600	248	6x6x6	18	400	50	2.002	3.535	2.002	3.524	3.163	4.505
G5W0	600	248	6x6x6	18	400	50	2.002	3.595	2.002	3.524	3.163	4.505
G0W0	600	150	4x4x4	18	400	50	1.993	3.349	2.002	3.363	2.783	4.605
G0W0	600	200	4x4x4	18	400	50	1.993	3.352	2.002	3.363	2.783	4.605
G0W0	600	248	4x4x4	9	400	50	1.993	3.356	2.002	3.363	2.783	4.605
G0W0	600	248	4x4x4	18	150	50	1.993	3.395	2.002	3.403	2.823	4.625
G0W0	600	248	4x4x4	18	200	50	1.993	3.371	2.002	3.363	2.803	4.605
G0W0	600	248	4x4x4	18	300	50	1.993	3.352	2.002	3.363	2.783	4.605
G0W0	600	248	4x4x4	12	400	50	1.993	3.356	2.002	3.363	2.783	4.605
G0W0	600	200	10x10x10	12	300	50	2.003	3.233	2.002	3.243	-	-
QPG3W0	600	200	6x6x6	12	300	50	2.002	3.573	2.002	3.684	3.323	4.665
QPG3W0	600	200	4x4x4	12	300	50	1.993	3.652	2.002	3.804	3.223	5.085
G0W0	600	200	4x4x4	12	300	50	1.993	3.347	2.002	3.363	2.783	4.605
G7W0	600	200	4x4x4	12	300	50	1.993	3.624	2.002	3.644	3.043	4.905
G0W0	600	200	6x6x6	12	300	50	2.002	3.267	2.002	3.283	2.903	4.224
G7W0	600	200	6x6x6	12	300	50	2.002	3.525	2.002	3.524	3.143	4.485
G0W0	600	200	4x4x4	12	300	50	1.993	3.352	2.002	3.363	2.783	4.605
G7W0	600	200	4x4x4	12	300	50	1.993	3.649	2.002	3.644	3.063	4.925
GW0	600	150	4x4x4	18	400	50	1.993	3.349	2.002	3.363	2.783	4.605
GW0	600	200	4x4x4	18	400	50	1.993	3.352	2.002	3.363	2.783	4.605
GW0	600	248	4x4x4	18	400	50	1.993	3.356	2.002	3.363	2.783	4.605
GW0	600	248	4x4x4	18	400	50	1.993	3.356	2.002	3.363	2.783	4.605
GW0	600	248	4x4x4	12	400	50	1.993	3.356	2.002	3.363	2.783	4.605
GW0	600	248	4x4x4	9	400	50	1.993	3.356	2.002	3.363	2.783	4.605
GW0	600	248	4x4x4	18	150	50	1.993	3.395	2.002	3.403	2.823	4.625
GW0	600	248	4x4x4	18	200	50	1.993	3.371	2.002	3.363	2.803	4.605
GW0	600	248	4x4x4	18	300	50	1.993	3.352	2.002	3.363	2.783	4.605
GW0	600	248	4x4x4	18	400	50	1.993	3.356	2.002	3.363	2.783	4.605

Table A.3: All GW and BSE calculation for ZnSe. The same abbreviations with Table A.2 are used.

GW flavor	EC	NBNDS	KPOINTS	NBNDSV	EC GW	NBNDSGW	EgDFT	EgGW	1st DFT p.	1st RPA p.	1st BSE p.	2nd BSE p.
QPG7W0	800	128	4x4x4	9	150	18	1.160	2.532	1.161	2.523	2.322	4.144
QPG7W0	1000	128	4x4x4	9	150	18	1.160	2.532	1.161	2.523	2.322	4.144
QPG7W0	600	128	4x4x4	18	150	27	1.160	2.584	1.161	2.603	2.382	4.184
QPG7W0	600	128	4x4x4	18	150	27	1.160	2.584	1.161	2.563	2.382	4.184
QPG7W0	800	128	4x4x4	18		27	1.160	2.589	1.161	2.563	-	-
QPG7W0	600	128	4x4x4	18	400	18	1.160	2.514	1.161	2.523	2.322	4.144
QPG7W0	600	300	4x4x4	9	150	18	1.160	2.244	1.161	2.523	2.322	4.124
QPG7W0	600	228	4x4x4	9	150	18	1.160	2.528	1.161	2.523	2.322	4.144
QPG7W0	600	128	4x4x4	9	150	36	1.160	2.616	1.161	2.603	2.422	4.224
QPG7W0	600	128	4x4x4	9	400	27	1.160	2.565	1.161	2.563	2.362	4.184
QPG3W0	600	560	4x4x4	18	150	27	1.160	2.806	1.161	2.923	2.483	4.304
QPG3W0	600	248	4x4x4	18	150	27	1.160	2.805	1.161	2.923	2.483	4.304
QPG3W0	600	248	4x4x4	18	150	50	1.160	2.856	1.161	3.003	2.543	4.344
QPG3W0	600	248	4x4x4	18	150	70	1.160	2.856	1.161	3.003	2.543	4.344
QPG3W0	600	248	4x4x4	18	400	50	1.160	2.849	1.161	2.843	2.402	4.204
QPG3W0	600	248	4x4x4	18	150	50	1.112	2.814	1.121	2.963	2.503	4.324
QPG3W0	600	248	4x4x4	18	400	50	1.125	2.849	1.121	3.003	2.543	4.364
QPG3W0	400	128	2x2x2	9	200	36	1.031	2.276	1.041	2.282	2.222	4.224
G7W0	600	250	8x8x8	18	400	50	1.173	2.516	1.161	2.523	-	-
G7W0	600	250	6x6x6	18	400	50	1.172	2.554	1.161	2.563	2.262	3.704
G0W0	600	200	4x4x4	12	300	50	1.160	2.427	1.161	2.442	1.962	3.784
G7W0	600	200	4x4x4	12	300	50	1.160	2.667	1.161	2.683	2.202	4.044
G0W0	600	200	6x6x6	12	300	50	1.172	2.336	1.161	2.322	2.042	3.484
G7W0	600	200	6x6x6	12	300	50	1.172	2.546	1.161	2.563	2.262	3.704
G0W0	600	200	4x4x4	12	350	50	1.160	2.430	1.161	2.442	1.982	3.810
G0W0	600	200	4x4x4	12	400	50	1.160	2.433	1.161	2.442	1.982	3.804
G0W0	600	200	4x4x4	18	300	50	1.160	2.427	1.161	2.442	1.962	3.784
G0W0	800	200	4x4x4	12	300	50	1.598	2.427	1.161	2.442	1.962	3.784
G0W0	600	200	4x4x4	12	300	50	1.160	2.427	1.161	2.442	1.962	3.784
G0W0	600	200	4x4x4	12	300	100	1.160	2.427	1.161	2.442	1.962	3.784

Table A.4: All GW and BSE calculations for ZnTe. The same abbreviations with Table A.2 are used.

GW flavor	EC	NBNDS	KPOINTS	NBNDSV	EC GW	NBNDSGW	EgDFT	EgGW	1st DFT p.	1st RPA p.	1st BSE p.	2nd BSE p.
QPG3W0	600	500	4x4x4	18	400	50	1.0589	2.0997	1.041	2.1622	1.8418	3.033
QPG3W0	800	248	4x4x4	18	400	50	1.059	2.1267	1.041	2.2022	1.8619	3.3033
QPG3W0	600	248	4x4x4	18	450	50	1.0589	2.1284	1.041	2.2022	1.8619	3.033
QPG3W0	600	248	4x4x4	27	400	50	1.0589	2.1265	1.041	2.2022	1.8619	3.033
QPG3W0	600	248	4x4x4	18	400	50	1.0589	2.1265	1.041	2.2022	1.8619	3.033
QPG3W0	800	500	4x4x4	18	400	50	1.059	2.0997	1.041	2.1622	1.8418	3.3033
QPG3W0	800	248	4x4x4	18	450	50	1.059	2.1286	1.041	2.2022	1.8619	3.3033
QPG3W0	800	248	4x4x4	27	450	50	1.059	2.1286	1.041	2.022	1.8619	3.3033
G0W0	600	480	4x4x4	18	400	50	1.0589	1.9201	1.041	1.9219	1.5816	2.963
QPG3W0	600	700	4x4x4	18	400	50	1.0589	2.0823	1.041	2.1622	1.8218	3.2833
G7W0	600	248	8x8x8	18	400	50	1.072	1.9434	1.0811	1.962	-	-
G7W0	600	248	6x6x6	18	400	50	1.0701	1.978	1.0811	1.962	1.7618	3.023
QPG3W0	800	288	4x4x4	18	450	50	1.059	2.1221	1.041	2.2022	1.8619	3.3033
QPG5W0	600	248	4x4x4	18	400	50	1.0589	2.1363	1.041	2.1221	1.7818	3.2232
QPG3W0	600	200	6x6x6	12	300	50	1.0589	2.133	1.041	2.2022	1.8619	3.3033
QPG3W0	600	200	4x4x4	12	300	50	1.0701	2.0402	1.0811	2.1221	1.9019	3.1632
G0W0	600	200	4x4x4	12	300	50	1.0589	1.9215	1.041	1.9219	1.5816	2.963
G7W0	600	200	4x4x4	12	300	50	1.0589	2.079	1.041	2.0821	1.7212	3.1431
G0W0	600	200	6x6x6	12	300	50	1.0701	1.8395	1.0811	1.8418	1.6216	2.8829
G7W0	600	200	6x6x6	12	300	50	1.0701	1.9816	1.0811	1.962	1.7618	3.023

APPENDIX B

More data on the Complex Zn-materials calculations.

Table B.1: Atom positions and primitive cells for the Hausmannite and spinel structures. 4a and 8a sites are tetrahedral and 8d and 16d sites are octahedral. For the x, y, z we used the experimental values of 0.3835, 0.25 and 0.375, respectively. Atom positions are given in fractional coordinates

Hausmannite			
		Cell	
A1	a	0	0
A2	0	a	0
A3	a/2	a/2	c/2
		Atom Positions (Fract. Coordinates)	
Mn (4a)	0	0	0
Mn (4a)	$-1/4$	$1/4$	$+1/2$
Mn (8d)	$+3/8$	$-3/8$	$+1/4$
Mn (8d)	$+3/8$	$+1/8$	$+1/4$
Mn (8d)	$-1/8$	$-3/8$	$-1/4$
Mn (8d)	$+3/8$	$-3/8$	$-1/4$
O (16h)	$-z$	$+(y-z)$	$2z$
O (16h)	$-z$	$-(y+z)$	$2z$
O (16h)	$-(y+z-3/4)$	$-(z-1/4)$	$(2z–1/2)$
O (16h)	$+(y-z-1/4)$	$-(z-1/4)$	$(2z–1/2)$
O (16h)	$+(z-1/4)$	$+(y+z-3/4)$	$-(2z–1/2)$
O (16h)	$+(z-1/4)$	$-(y-z-1/4)$	$-(2z–1/2)$
O (16h)	$y+z$	z	$-2z$
O (16h)	$-y+z$	z	$-2z$
Spinel Mn_2NiO_4			
		Cell	
A1	a/2	a/2	0
A2	a/2	0	a/2
A3	0	a/2	a/2
		Atom Positions (Fract. Coordinates)	
Ni (8a)	$-1/8$	$-1/8$	$-1/8$
Ni (8a)	$+1/8$	$+1/8$	$+1/8$
Mn (16d)	$+1/2$	$+1/2$	$+1/2$
Mn (16d)	0	$+1/2$	$+1/2$
Mn (16d)	$+1/2$	0	$+1/2$
Mn (16d)	$+1/2$	$+1/2$	0
O (32e)	x	x	x
O (32e)	$(1/2 - 3x)$	x	x
O (32e)	x	$(1/2 - 3x)$	x
O (32e)	x	x	$(1/2 - 3x)$
O (32e)	$-x$	$-x$	$-x$
O (32e)	$-(1/2 - 3x)$	$-x$	$-x$
O (32e)	$-x$	$-(1/2 - 3x)$	$-x$
O (32e)	$-x$	$-x$	$-(1/2 - 3x)$

Table B.2: Random magnetization runs for the 16 atom primitive cell along with more conventional magnetic moment guesses for reference. Magnetic moments are all in μ_B

Initial Guesses						Relaxed/Converged State						
Mn	Mn	Mn	Mn	Ni	Ni	Mn	Mn	Mn	Mn	Ni	Ni	Energy(eV)
5	5	5	5	-5	-5	3.54	3.54	3.54	3.54	-1.12	-1.12	-106.04
9.7	3.6	2.2	-4.6	0.0	5.3	3.35	3.35	3.34	-3.43	-1.15	1.05	-105.77
8.8	-5.7	-8.0	3.3	-4.1	-2.2	3.48	-3.1	-3.15	3.49	-1.17	-0.92	-105.76
3.3	-9.8	4.5	-1.2	-5.0	-1.1	3.47	-3.14	3.47	-3.15	-1.03	-1.03	-105.76
-4.2	7.6	1.3	-6.7	1.2	-7.9	-3.14	3.47	3.47	-3.14	-1.03	-1.03	-105.76
5	5	-5	-5	-5	5	3.35	3.36	-3.35	-3.36	-1.04	1.04	-105.74
-5	5	5	-5	-5	5	-3.35	3.35	3.36	-3.36	-1.04	1.04	-105.74
5	-5	5	-5	-5	5	3.35	-3.35	3.36	-3.36	-1.04	1.05	-105.74
-5	5	-5	5	-5	5	-3.35	3.35	-3.36	3.36	-1.04	1.05	-105.74
-0.7	8.4	6.1	0.9	-5.9	-7.5	0.19	3.5	3.5	3.48	-1.26	-1.29	-105.36
5	5	5	5	5	5	3.24	3.24	3.26	3.26	1.22	1.22	-105.04
9.4	-0.2	1.0	-3.1	-10.0	6.8	3.36	-3.34	0.01	-3.34	-1.04	1.1	-104.99
6.6	-2.4	9.3	6.5	-7.7	5.5	3.34	0.39	3.34	3.34	-1.19	0.86	-104.86
-3.6	-10.0	2.1	3.4	-10.0	-8.3	-3.08	-3.08	-0.12	3.44	-0.9	-0.89	-104.81

```
############################################################################## Data Processing

## Mn exchanged combinations

s = 16
mn = 16-s
combs = np.array(list(itr.combinations(pos,s)))


repeats = np.array(list(itr.product([lc,-lc,0],repeat = 3)))  ### Repeats of the primitive cell
distances = []

uni_combs = []

for i in range(len(combs)):          #### Parse through possible combinations

    subs = []       # Store one iteration's substituted coordinate arrays
    dist = []       # Store one iteration's minimum distances of substituted atoms here
#    symdist = []    # Store all the distances for the repeats here


    for j in range(len(combs[0])):                    #### Parse through data points in combination and store them for this combination
        subs.append(combs[i,j])
    pairs = np.array(list(itr.combinations(subs,2)))    #### Find all the data point pairs

    ##At this point I want to find all the minimum distances between the substituted atoms
    for p in range(len(pairs)):                                    #### Parse through possible pairs and measure distances
        symdist = []
        for r in range(len(repeats)):                                  #### Include symmetric repeats of the second atom
            d = distance(pairs[p,0], pairs[p,1]+repeats[r])
            symdist.append(d)
        dist.append(((((min(symdist))*100) // 1 )/100)   ## Store the distance between every pair

    ### Now all the distances between pairs has been stored, but there are a lot of pairs that are effectively identical
    ### so we need to store only the ones that are unique and extract the pair coordinate array
    dist.sort()

    if dist not in distances:   ##Logical operation to filter dublicate interactions
        distances.append(dist)
        uni_combs.append(subs)



    ##For naming/organizational purpuses we are going to count first, second and third neighboor Zn-Zn interactions in each configuration
    fn = 0
    sn = 0
    tn = 0
    for g in dist:
        if g == 2.95:
            fn = fn +1
        elif g == 5.11:
            sn = sn +1
        elif g == 5.9:
            tn = tn+1


############################################################################## Make POSCAR files
    filen = open("POSCAR_fn%d_sn%d_tn%d" % (fn,sn,tn),  "w")
```

Figure B.1: The code used to find all the unique configurations for the various substitutions of Zn in Mn_2NiO_4. The code was written in Python 3.8

List of Figures

List of Tables

Bibliography

[1] J. Wang, R. Chen, L. Xiang, and S. Komarneni, "Synthesis, properties and applications of ZnO nanomaterials with oxygen vacancies: A review," *Ceramics International*, vol. 44, no. 7, pp. 7357 – 7377, 2018.

[2] A. D. Mauro, M. E. Fragalà, V. Privitera, and G. Impellizzeri, "ZnO for application in photocatalysis: From thin films to nanostructures," *Materials Science in Semiconductor Processing*, vol. 69, pp. 44 – 51, 2017. ZnO-based materials and applications.

[3] Q. Zhang, H. Li, Y. Ma, and T. Zhai, "ZnSe nanostructures: Synthesis, properties and applications," *Progress in Materials Science*, vol. 83, pp. 472 – 535, 2016.

[4] J. Zhou, H. L. Zhuang, and H. Wang, "Layered tetragonal zinc chalcogenides for energy-related applications: from photocatalysts for water splitting to cathode materials for li-ion batteries," *Nanoscale*, vol. 9, pp. 17303–17311, 2017.

[5] C. Panchal, A. Opanasyuk, V. Kosyak, M. Desai, and I. Protsenko, "Structural and substructural properties of the zinc and cadmium chalcogenides thin films (a review)," *Journal of Nano- and Electronic Physics*, vol. 3, no. 1 PART2, pp. 274–301, 2011.

[6] K. Aruchamy, R. Nagaraj, H. M. Manohara, M. R. Nidhi, D. Mondal, D. Ghosh, and S. K. Nataraj, "One-step green route synthesis of spinel $ZnMn_2O_4$ nanoparticles decorated on MWCNTs as a novel electrode material for supercapacitor," *Materials Science and Engineering: B*, vol. 252, p. 114481, 2020.

[7] Y. Deng, L. Wan, Y. Xie, X. Qin, and G. Chen, "Recent advances in Mn-based oxides as anode materials for lithium ion batteries," *RSC Adv.*, vol. 4, pp. 23914–23935, 2014.

[8] G. Sivaprakash, K. Mohanrasu, V. Ananthi, M. Jothibasu, D. D. Nguyen, B. Ravindran, S. W. Chang, P. Nguyen-Tri, N. H. Tran, M. Sudhakar, K. Gurunathan, S. Arokiyaraj, and A. Arun, "Biodiesel production from ulva linza, ulva tubulosa, ulva fasciata, ulva rigida, ulva reticulate by using Mn_2NiO_4 heterogenous nanocatalysts," *Fuel*, vol. 255, p. 115744, 2019.

[9] G. C. de Györgyfalva] and I. Reaney, "Decomposition of NiMn2O4 spinel: an NTC thermistor material," *Journal of the European Ceramic Society*, vol. 21, no. 10, pp. 2145 – 2148, 2001.

[10] R. Schmidt, A. Basu, and A. W. Brinkman, "Small polaron hopping in spinel manganates," *Phys. Rev. B*, vol. 72, p. 115101, Sep 2005.

[11] E. N. Economou, *Solid State Physics: A shortened version*. Crete University Press, 2 ed., 2017.

[12] J. Thijssen, *Computational Physics*. Cambridge University Press, 2 ed., 2007.

[13] P. Hohenberg and W. Kohn, "Inhomogeneous electron gas," *Phys. Rev.*, vol. 136, pp. B864–B871, Nov 1964.

[14] W. Kohn and L. J. Sham, "Self-consistent equations including exchange and correlation effects," *Phys. Rev.*, vol. 140, pp. A1133–A1138, Nov 1965.

[15] J. P. Perdew, K. Burke, and M. Ernzerhof, "Generalized gradient approximation made simple," *Phys. Rev. Lett.*, vol. 77, pp. 3865–3868, Oct 1996.

[16] M. Shishkin and G. Kresse, "Self-consistent GW calculations for semiconductors and insulators," *Phys. Rev. B*, vol. 75, p. 235102, Jun 2007.

[17] L. Hedin, "New method for calculating the one-particle Green's function with application to the electron-gas problem," *Phys. Rev.*, vol. 139, pp. A796–A823, Aug 1965.

[18] M. S. Hybertsen and S. G. Louie, "First-principles theory of quasiparticles: Calculation of band gaps in semiconductors and insulators," *Phys. Rev. Lett.*, vol. 55, pp. 1418–1421, Sep 1985.

[19] G. Onida, L. Reining, and A. Rubio, "Electronic excitations: density-functional versus many-body Green's-function approaches," *Rev. Mod. Phys.*, vol. 74, pp. 601–659, Jun 2002.

[20] M. C. Payne, M. P. Teter, D. C. Allan, T. A. Arias, and J. D. Joannopoulos, "Iterative minimization techniques for ab initio total-energy calculations: molecular dynamics and conjugate gradients," *Rev. Mod. Phys.*, vol. 64, pp. 1045–1097, Oct 1992.

[21] P. E. Blöchl, "Projector augmented-wave method," *Phys. Rev. B*, vol. 50, pp. 17953–17979, Dec 1994.

[22] L. Ley, R. Pollak, F. McFeely, S. Kowalczyk, and D. Shirley, "Total valence-band densities of states of III-V and II-VI compounds from x-ray photoemission spectroscopy," *Physical Review B*, vol. 9, pp. 600–621, 01 1974.

[23] Y.-M. Yu, S. Nam, O. Byungsung, K.-S. Lee, Y. Choi, J. Lee, and P. Yu, "Variation of band gap energy and photoluminescence characteristics with Te composition of ZnS 1-x Te x epilayers grown by hot-wall epitaxy," *Applied Surface Science*, vol. 182, no. 1-2, pp. 159–166, 2001.

[24] M. Cardona and G. Harbeke, "Optical properties and band structure of wurtzite-type crystals and rutile," *Physical Review*, vol. 137, no. 5A, pp. A1467–A1476, 1965.

[25] M. Aven, D. Marple, and B. Segall, "Some electrical and optical properties of ZnSe," *Journal of Applied Physics*, vol. 32, no. 10, pp. 2261–2265, 1961.

[26] W. Woody and J. Meese, "Photoluminescence of ZnTe," *Journal of Applied Physics*, vol. 47, no. 8, pp. 3640–3643, 1976.

[27] W. Luo, S. Ismail-Beigi, M. L. Cohen, and S. G. Louie, "Quasiparticle band structure of ZnS and ZnSe," *Phys. Rev. B*, vol. 66, p. 195215, Nov 2002.

[28] A. Riefer, N. Weber, J. Mund, D. Yakovlev, M. Bayer, A. Schindlmayr, C. Meier, and W. Schmidt, "Zn-VI quasiparticle gaps and optical spectra from many-body calculations," *Journal of Physics Condensed Matter*, vol. 29, no. 21, 2017.

[29] S. Khidzir, F. Maulida, and W. Wan Abdullah, "*gw* approximation study of the compton profile of ZnSe," *Radiation Effects and Defects in Solids*, vol. 172, no. 7-8, pp. 664–677, 2017.

[30] H. Venghaus, "Valence-band parameters and g factors of cubic zinc selenide derived from free-exciton magnetoreflectance," *Physical Review B*, vol. 19, no. 6, pp. 3071–3082, 1979.

[31] Y.-M. Yu, S. Nam, K.-S. Lee, Y. D. Choi, and B. O, "Photoluminescence characteristics of ZnTe epilayers," *Journal of Applied Physics*, vol. 90, no. 2, pp. 807–812, 2001.

[32] P. Villars and L. D. Calvert, *Pearson's handbook: crystallographic data for intermetallic phases Vol. I*, p. 4347. ASM International, 1991.

[33] J.-R. Huang, H. Hsu, and C. Cheng, "Strongly reduced band gap in $NiMn_2O_4$ due to cation exchange," *Journal of Magnetism and Magnetic Materials*, vol. 358-359, pp. 149 – 152, 2014.

[34] R. Arras, T. Ly Le, S. Guillemet-Fritsch, P. Dufour, and C. Tenailleau, "First-principles electronic structure calculations for the whole spinel oxide solid solution range $Mn_xCo_{3-x}O_4$ ($0 < x < 3$) and their comparison with experimental data," *Physical Chemistry Chemical Physics*, vol. 18, no. 37, pp. 26166–26176, 2016.

[35] C. Franchini, R. Podloucky, J. Paier, M. Marsman, and G. Kresse, "Ground-state properties of multivalent manganese oxides: Density functional and hybrid density functional calculations," *Phys. Rev. B*, vol. 75, p. 195128, May 2007.

[36] A. Chartier, P. D'Arco, R. Dovesi, and V. R. Saunders, "Ab initio hartree-fock investigation of the structural, electronic, and magnetic properties of Mn_3O_4," *Phys. Rev. B*, vol. 60, pp. 14042–14048, Nov 1999.

[37] R. W. G. Wyckoff, *The structure of Crystals Vol. 2-3*, pp. 79–87. John Wiley and Sons, 2 ed., 1991.